Detecting dynamic domains and local fluctuations in complex molecular systems via timelapse neighbors shuffling

Detecting dynamic domains and local fluctuations in complex molecular systems *via* timelapse neighbors shuffling

Martina Crippa[a], **Annalisa Cardellini**[b], **Cristina Caruso**[a], **and Giovanni M. Pavan**[a,b,*]

[a]Department of Applied Science and Technology, Politecnico di Torino, Corso Duca degli Abruzzi 24, 10129 Torino, Italy; [b]Department of Innovative Technologies, University of Applied Sciences and Arts of Southern Switzerland, Polo Universitario Lugano, Campus Est, Via la Santa 1, 6962 Lugano-Viganello, Switzerland

This manuscript was compiled on July 25, 2023

It is known that the behavior of many complex systems is controlled by local dynamic rearrangements or fluctuations occurring within them. Complex molecular systems, composed of many molecules interacting with each other in a Brownian storm, make no exception. Despite the rise of machine learning and of sophisticated structural descriptors, detecting local fluctuations and collective transitions in complex dynamic ensembles remains often difficult. Here we show a machine learning framework based on a new descriptor, which we name Local Environments and Neighbors Shuffling (LENS), that allows identifying dynamic domains and detecting local fluctuations in a variety of systems in an abstract and efficient way. By tracking how much the microscopic surrounding of each molecular unit changes over time in terms of neighbor individuals, LENS allows to characterize the global (macroscopic) dynamics of molecular systems in phase-transition, phases-coexistence, as well as intrinsically characterized by local fluctuations (*e.g.*, defects). Statistical analysis of the LENS time-series data extracted from molecular dynamics trajectories of, *e.g.*, liquid-like, solid-like, or dynamically-diverse complex molecular systems allows tracking in an efficient way the presence of different dynamic domains and of local fluctuations emerging within them. The approach is found robust, versatile, and applicable independently of the features of the system and simply provided that a trajectory containing information on the relative motion of the interacting units is available. We envisage that "such a LENS" will constitute a precious basis for exploring the dynamic complexity of a variety of systems and, given its abstract definition, not necessarily of molecular ones.

Descriptor | Complex molecular systems | Local fluctuations | Dynamic environments | Machine-learning |

Supramolecular assemblies and crystalline structures, are characterized by a non-trivial internal dynamics that is often ambiguous and challenging to unveil.(1–5) Self-assembled structures, composed of molecular units interacting with each other *via* reversible non-covalent interactions, offer a notable example of systems where a continuous reshuffling and exchange of the constitutive building-blocks is at the origin of interesting bioinspired and stimuli-responsive properties.(6–13) Also other completely different systems, such as, *e.g.*, metallic structures, are known to possess a non-trivial internal dynamics. Already at $\sim 1/3$ of the melting temperature (*i.e.*, the so-called Hüttig temperature) metal surfaces are known to enter a dynamic equilibrium where atoms may leave their lattice positions and start moving on the atomic surface, inducing surface transformations and reconstructions.(5, 14, 15) In nanosized metal systems (metal nanoclusters, nanoparticles, etc.), such atomic dynamics emerges even at lower (*e.g.*, room) temperature.(16) In all these cases, the dynamics and fluctuations in time of the building blocks are deeply connected to important properties of the materials, such as, *e.g.*, the mechanical properties of metals,(17–19) their performance in heterogeneous catalysis,(20–23) or, for example, the dynamics adaptivity and stimuli-responsiveness of supramolecular materials.(13, 24–27) Gaining the ability to track the dynamics of the building blocks in complex self-organizing molecular systems is fundamental to studying and rationalizing most of their properties.(6, 27–31) However, this is also typically challenging and demands efficient analysis approaches.

Molecular dynamics (MD) simulations are being increasingly used to obtain high-resolution insights into the behavior of a variety of systems.(32) (1, 33–40) One key advantage of MD trajectories is that these keep track of the motion of the individual molecular units and contains all phase-space information, hence the complete structure and dynamics of the complex system. Nonetheless, non-trivial aspects concern the extraction of relevant information from the large amount of data contained in the MD trajectories and their conversion to human-readable form. Typical descriptors used to extract information from MD trajectories may be divided into system-specific or abstract (general) descriptors. Extensively used to investigate, *e.g.*, ice-water systems,(41) or metal clusters,(38, 42) to cite a few examples, *ad hoc* descriptors

Significance Statement

Many complex systems are controlled by local fluctuations triggering collective motions and rearrangements. Rapid direction changes in bird-flocks or fish-banks are a few examples but, even on the smallest scales, complex molecular systems make no-exception. Local variations in microscopic molecular environments are at the origin of, *e.g.*, phase-transitions, nucleation phenomena, and dynamic phases equilibria, but they are also typically difficult to detect. Here we show a new descriptor, named Local Environments and Neighbors Shuffling (LENS), which allows tracking local fluctuations and unveiling the dynamic complexity of a variety of molecular systems. Analysis of time-series LENS data provides a unique insight into innately dynamic molecular ensembles and we envisage will offer interesting perspectives on the behavior of complex systems in general.

G.M.P. conceived this research and supervised the work. M.C. developed the LENS descriptor and performed the analyses. M.C., A.C., and C.C. performed the simulations. All authors analyzed and discussed the results. M.C., A.C., and G.M.P. wrote the manuscript.

The authors declare no competing interests.

*To whom correspondence should be addressed. E-mail: giovanni.pavan@polito.it

build on considerable *a priori* knowledge of the system under consideration and are developed and optimized on such specific system, but poorly transferable to different ones. Abstract descriptors *e.g.*, Smooth Overlap of Atomic Positions (SOAP), radial distribution functions ($g(r)$), etc. are conversely less specific and more general.(41, 43–49) Although less precise than the tailored ones, abstract descriptors offer an advantage in terms of transferability: they can be applied to different systems and do not require deep *a priori* knowledge of the system's features.(43, 48, 50) The high-dimensional data obtained using such descriptors are typically converted into lower-dimensional human-readable information *via* supervised and unsupervised machine learning (ML) approaches (*e.g.*, clustering), and analyzed to characterize the internal dynamics of the studied systems.(51–57) For example, unsupervised clustering of SOAP(43) data extracted from MD trajectories recently allowed to study the complex dynamics in self-assembling fibers, micelles, lipid bilayers, (47, 50, 58–60) in confined ionic environments,(47, 59) as well as in metal nanoparticles and surfaces.(5, 16)

Despite the advantages granted by such ML developments, the behavior of complex molecular systems is often determined by rare fluctuations and local dynamic rearrangements,(6, 7, 27) poorly captured by average-based measurements. The dynamics of defects in materials science is a typical example of local events determining a variety of hierarchical materials' properties.(31, 61) However, detecting and tracking local fluctuations becomes increasingly difficult when dealing with complex molecular/atomic systems where a certain degree of structural order is coupled with a continuous exchange and reshuffling of molecules/atoms.(25) Abstract descriptors that are transferable and at the same time effective in capturing local fluctuations in complex dynamic systems would be fundamental.

Here we develop an abstract descriptor named "Local Environments and Neighbors Shuffling (LENS)". Combined with a ML-based analysis, LENS is capable of detecting different dynamic domains and tracking local fluctuations in complex molecular systems without deep prior knowledge of the chemical/physical features of the constituent building blocks but simply by tracing their reciprocal motion and instantaneous fluctuations in space and time. LENS builds on a relatively simple definition and can be transferred to a variety of complex systems with, liquid, solid, or diverse/hybrid dynamics (*e.g.*, typical of phase-transitions). The results obtained with LENS change the vision of complex molecular systems and, building on simple and general basic concepts, suggest a broad applicability (*e.g.*, not necessarily restricted to molecular ones).

Results

LENS: Local Environments & Neighbors Shuffling. In this work, we analyze molecular dynamics (MD) trajectories of various molecular/atomic systems, from soft to crystalline ones, possessing liquid-like to solid-like dynamics. As examples of fluid-like systems, we use lipid bilayers and surfactant micelles, (60) while for solid-like dynamics, we focus on metal surfaces(5) and nanoparticles.(16) Furthermore, we also include systems with intrinsically non-uniform internal dynamics, such as, *e.g.*, a system where ice and liquid water coexist in dynamic equilibrium in correspondence of the solid-liquid transition, and soft self-assembled fibers whose behavior is dominated by local dynamic defects (see Supplementary Table S1 for system details).(6, 7, 50) Such a large diversity is functional to test the generality of our approach.

Despite their intrinsic differences, all these systems can be considered from an abstract point of view as composed of N dynamically interacting particles with their own individual trajectories. The analysis approach we present herein is based on the concept of molecular individuals (even in cases of systems of chemically identical particles). In particular, from the global trajectory of the system, we can identify the sub-trajectory of the ith particle (with i ranging from 1 to N). From this, we can thus describe the local environment surrounding each ith particle in terms of its neighbor individuals (IDs) and monitor the changes of IDs at each interval between the sampled timestep Δt along the trajectory. Figure 1a (top-left) shows a representative scheme where, at a given time t, the neighbor ID units (gray circles) surrounding the ith particle ($i = 1$ – red circle) within a sphere of radius r_{cut} (namely, the neighborhood cutoff) are listed in a fingerprint string $C^t_{i=1}$. The local $C^{t+\Delta t}_{i=1}$ environment at $t + \Delta t$ may change from that one at time t ($C^t_{i=1}$) when neighbor switching (Figure 1a: top-right), addition (Figure 1a: bottom-left), or subtraction (bottom-right) occur in Δt.

Our analysis is based on monitoring the time-lapse sequence of the ID data along a given trajectory. We developed a new descriptor named "Local Environments and Neighbors Shuffling (LENS)", which allows us to track to what extent the ith local environment changes at every consecutive time interval (C^t_i, $C^{t+\Delta t}_i$, $C^{t+2\Delta t}_i$, etc.) along its trajectory. LENS is built to detect essentially two types of changes in the local neighbor environments along a trajectory: (i) changes in the number of neighbors (addition/leave of one or more neighbors), and/or (ii) changes in the IDs of the neighbors (switching of one or more neighbor IDs). The instantaneous value of LENS (δ_i, in its variable form) is defined as:

$$\delta_i^{t+\Delta t} = \frac{\#(C_i^t \bigcup C_i^{t+\Delta t} - C_i^t \bigcap C_i^{t+\Delta t})}{\#(C_i^t + C_i^{t+\Delta t})} \qquad [1]$$

where the first ($C_i^t \bigcup C_i^{t+\Delta t}$) and the second term ($C_i^t \bigcap C_i^{t+\Delta t}$) of the numerator are respectively the mathematical union and intersection of the neighbor IDs present within r_{cut} from particle i at time t and at time $t + \Delta t$. The denominator contains a normalization factor, which is the total length of the neighbor ID lists (strings) at the two consecutive timesteps. Thus, for every particle i, the $\delta_i(t)$ ranges from 0 to 1 for local neighbor environments which are respectively persistent to highly dynamic over time. For example, in the hypothetical case where no local neighbor changes occur in Δt, the union of C_i^t and $C_i^{t+\Delta t}$ is identical to their intersection, and LENS gives $\delta_i^{t+\Delta t} = 0$. In a case where, *e.g.*, all IDs permute in different IDs in Δt (complete shuffling while the number of neighbors remains constant), the numerator of the δ_i^t ($(C_i^t + C_i^{t+\Delta t}) - 0$) is equal to the denominator, and LENS gives $\delta_i^{t+\Delta t} = 1$. As shown in Figure 1b (top), the LENS signal (δ_i) for the generic particle i can be considered proportional to the local neighborhood changes within a time-interval Δt. Figure 1b reports two examples of LENS signal over time in the cases of a particle with fluid-like behavior (center) and of another particle (bottom) which dynamics is dominated by local fluctuations.

The time-lapse analysis provided by LENS can be also

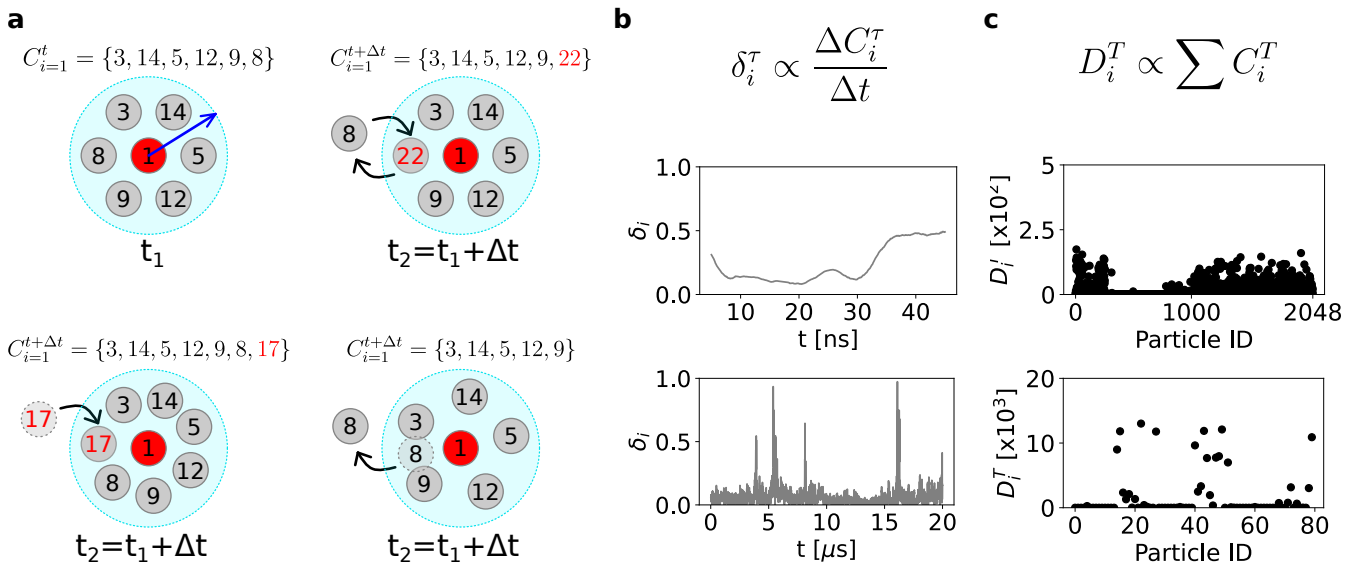

Fig. 1. Tracking local neighbor environments in complex molecular systems with the LENS descriptor. (a) The local molecular environment of the particle $i = 1$ at time t is defined by an array C_i^t containing the identities (IDs) of all molecular units within a sphere of radius r_{cut} (blue arrow). Along the MD trajectory, C_i^t can be calculated for all constitutive particles at each sampled MD timestep t. The local molecular environment C_i^t of the unit $i = 1$ (red particle) at time t_1 (top-left). The local environment $C_i^{t+\Delta t}$ at time $t_2 = t_1 + \Delta t$, when particle switching occurs in Δt (top-right). The local environment $C_i^{t+\Delta t}$ at time $t_2 = t_1 + \Delta t$, when one particle enters (bottom-left) or leaves (bottom-right) the neighborhood sphere in Δt. (b) The LENS descriptor. The LENS signal for the generic particle i δ_i^τ is proportional to the number of changes in the neighborhood within a timestep τ (top). Two examples of typical LENS signals, $\delta_i(t)$ (raw data smoothed as described in the Methods section), for a particle with fluid-like behavior (center) and a particle with dynamics dominated by local fluctuations (bottom). (c) Global statistical analysis. All contact events between the particle i and all the others in the system, visited along the entire trajectory T, are counted and listed in the D_i^T array. Two examples of contact counts, D_i^T, between a molecule i and all other IDs in the two distinct dynamics cases of panel (c).

corroborated/compared with a time-independent statistical analysis of the ID neighbor list data C_i. In particular, from the ID neighbor list data C_i calculated at every sampled time-step (t, $t + \Delta t$, $t + 2\Delta t$, etc.), one can easily estimate how many times a particle i has been in direct contact with all the other N ID particles during a sampled trajectory T. All inter-IDs contacts visited along the trajectory T are then stored into an array D_i^T (Figure 1*c*). In such global statistical analysis, the D_i^T data are useful to detect the presence of domains differing from each other in terms of dinamicity/persistence of the local neighbor individuals over time (*i.e.*, in terms of how quickly/slowly the neighbor IDs change along the trajectory). In particular, analysis of the global D^T contact matrix (Figure 2e) provides information on the propensity of a certain i unit to be, *e.g.*, persistently surrounded by the same neighbors (IDs) or by a population that is in continuous reshuffling during the simulation (see Methods for details).

To provide a more quantitative investigation, we define a *Variability* (V) parameter by estimating the standard deviation of the D_i^T counts. Namely, high standard deviation of the D_i^T values means that, among all sampled timesteps, a generic unit i shows a high number of contact events with few neighbors and very low contact occurrence with the others (meaning that its closest neighbors tend to remain always the same along the trajectory). On the other hands, low standard deviation of the D_i^T values implies a moderate but uniform number of neighboring events among all neighbor IDs (meaning that the closest neighbors of unit i change a lot along the trajectory). In this perspective, the *Variability* (V) parameter is then defined as the inverse of the standard deviation of the D_i^T values: more dynamic neighborhood environments of i have high V while more static neighborhood environments have low V values.

As it will be discussed in the next sections, such global time-independent analysis does correlate with the LENS one for systems composed of statistically-relevant dynamically-diverse domains (populated by a relevant number of units that can be effectively detected *via* "dynamic-pattern recognition" approaches), while it does not for systems whose dynamics is dominated by sparse local fluctuations/transitions.

Into the dynamics of fluid-like systems. We start testing LENS on a soft molecular system with non-trivial fluid-like dynamics (Figure 2). In particular, we analyze a MD simulation trajectory of a coarse-grained (CG) bicomponent lipid bilayer composed of 1150 **DIPC**:**DPPC** lipid molecules in 2:3 ratio (see Figure 2a, where **DIPC** and **DPPC** are colored in red and blue respectively). It is well known that at $T = 280$ K, a 2:3 **DIPC**:**DPPC** lipid bilayer self-segregates into two distinct regions, populated by the two lipid species which do not mix in such conditions.(62) For this lipid model we ran 15 μs of CG-MD simulation using the Martini 2.2 force field,(63) (see Methods section and Supplementary Table S1 for details). The last 10 μs, representative of an equilibrated MD regime, are used for the analysis.

Being interested in the lipid shuffling dynamics, in our LENS analysis we use the lipid heads as reference constituent particles and we set a time-interval of $\Delta t = 10$ ns with a neighborhood cutoff $r_{cut} = 16$ Å (Supplementary Figure S2). On average, with such a setup, every reference lipid has ~ 13 neighbors. Noteworthy, the robustness of the analysis while changing the r_{cut} or Δt is demonstrated in Supplementary Figures S3,S4. Figure 2b shows on the left the time-profiles of $\delta_i(t)$ for the 1150 lipid heads forming the bilayer, while on the right the δ_i data distribution and the correlated KDE are reported.

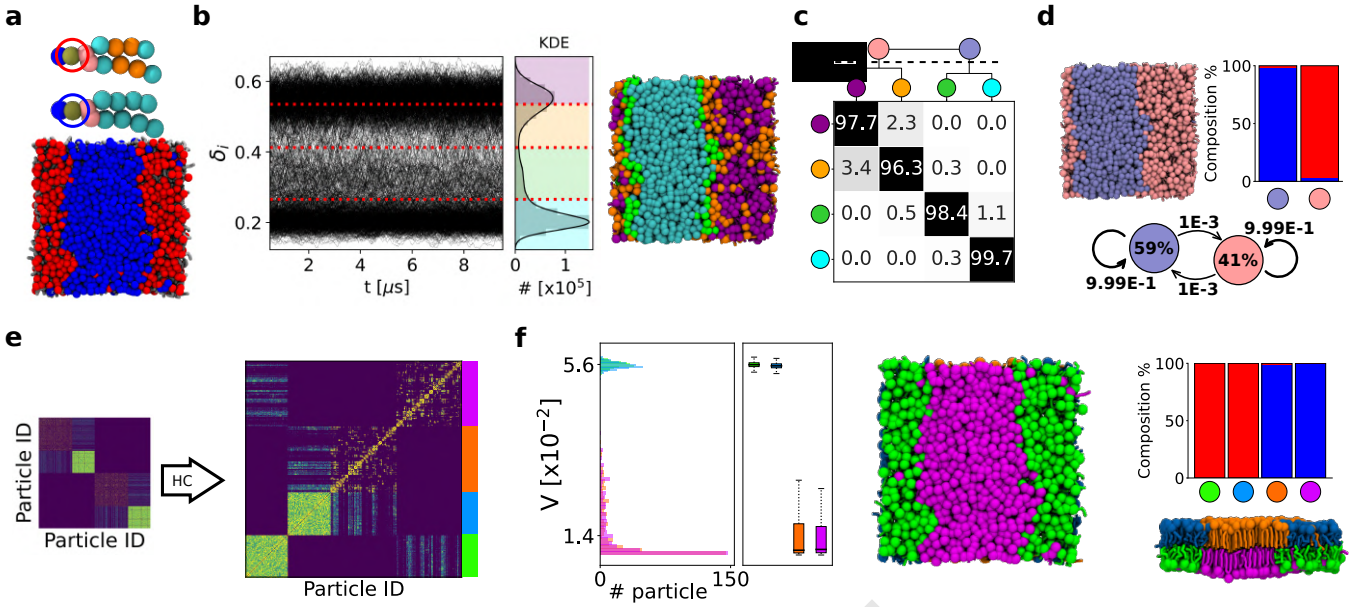

Fig. 2. LENS analysis of fluid-like systems. (a) Bicomponent lipid bilayer made of 1150 lipid molecules, namely **DIPC**:**DPPC** in 2:3 ratio (460:690 in total, 230:345 per leaflet) colored in red and blue, respectively. (b) Time-series of LENS signals, $\delta_i(t)$, with the Kernel Density Estimate (KDE) of LENS distribution classified into four clusters (left). MD snapshot of lipids bilayer colored according to their clusters of belonging (right). (c) Inter-clusters normalized transition probability matrix. The p_{ii} and p_{ij} matrix entries indicate the % probability that molecules with LENS signal typical of a cluster i remain in that dynamical environment or move to another one j (with different dynamics) in Δt. Hierarchical grouping of the dynamically-closer clusters (dendrogram cutting) is reported on top of the matrix, and it provides two macroclusters, merging cyan and green on one hand, and orange and purple on the other hand. (d) MD snapshot of lipid bilayer colored according to macroclusters in (c): light-blue identifying **DPPC** lipids, pink identifying **DIPC** lipids (top-left). Cluster composition histogram (top-right) and interconversion diagram (bottom) with the transition exchange probabilities and the cluster population percentages (within colored circle). (e) HC analysis of the D^T matrix identifying four main clusters (light blue, green, purple, orange). (f) *Variability*, V, analysis of the clusters: distributions, median (first and third quartiles), maximum and minimum values (whiskers). The green and light blue clusters, arranging on separated bilayer leaflets, have higher V than the orange and magenta clusters (left). MD snapshot front view of lipid bilayer colored according the HC clustering of D^T matrix (middle). Cluster composition histogram (top-right): the green and light blue clusters are made of **DIPC** lipids (in red in (a)), while the orange and magenta ones correspond to the **DPPC** lipids (in blue in (a)). MD snapshot lateral view of lipid bilayer colored according the HC clustering of D^T matrix (bottom-right).Note that the sub-units within each considered system are illustrated coherently to the color code of the belonging cluster.

Here, two peaks are clearly detected. A simple supervised clustering analysis, carried out with the KMeans algorithm(64) on LENS signals, demonstrates that the δ_i distribution can be classified into four clusters (cyan, green, orange, and purple) denoted as dynamical clusters or domains. The time-series data of the individual lipid IDs along the trajectory allows computing the exchange probability matrix represented in Figure 2c and obtaining the associated dendrogram detailing the hierarchical interconnection/adjacency between such four detected clusters. In the exchange probability matrix, the p_{nn} and p_{nm} entries indicate the % probability for a lipid i belonging to a given dynamical cluster n – having a characteristic rate-of-change of its local neighbor environment – to remain in that dynamic domain or to undergo a transition into a different dynamic cluster m – with a different LENS fingerprint – in Δt (see Methods for additional details). The four obtained microclusters can be then hierarchically merged based on the dendrogram in Figure 2c, by connecting those having a high probability of exchanging molecules. Such approach provides two main macroclusters, colored in light blue and pink, whose populations and transition probabilities in Δt are reported in the interconversion diagram of Figure 2d within circles and on the arrows, respectively.

The data show that the pink domain, obtained after merging orange and purple clusters, is dominated by those lipid units having a higher aptitude to mutate their neighborhood environment: in other words, by those having a more dynamic local neighbor environment (high δ_i). On the other hand, the lipids belonging to the light blue domain, resulting from blending the cyan and green microclusters, reveal a slower variation of their surrounding environment and hence weaker local mobility (low δ_i). Not surprisingly, while the pink dynamics domain overlaps with the **DIPC** molecules (red component), known to be in liquid phase (62), the light blue cluster matches up with the **DPPC** lipids (blue component) that are instead in gel phase (62) (see composition histogram in Figure 2d, top-right). Furthermore, the estimated exchange probabilities between the pink and light blue macroclusters are very low ($< 1\%$) in $\Delta t = 10$ ns, which is consistent with a sharp segregation between the gel and fluid phases.

In order to test the robustness of our descriptor LENS, we have also carried out a 2D Voronoi-based tessellation (a reference approach to detect, *e.g.*, liquid/gel phases in lipid bilayers (65)) on the MD trajectories of the **DIPC-DPPC** lipid bilayer at $T = 280$ K. The obtained results show how, in the case of phase segregation in the **DIPC-DPPC** bilayer, the Voronoi analysis while qualitatively matching with the results obtained with LENS, reports a less well defined and more blurred characterization of the liquid **DIPC** and gel **DPPC** segregated phases that are expected experimentally (62) (see Supplementary Figure S15).

We also tested the robustness of the LENS results against tuning the Δt (i.e., the time resolution) in the analysis (see Figure S4). Comparing the results of Figure S4a and S4b, it is

possible to note that the absolute values of LENS – which are related to the degree of reshuffling in the microscopic neighbor environments in the Δt – may differ while changing the sampling time-step. This is expected, as changing the Δt in these analyses equals to changing the time-resolution and the details that are consequently captured (i.e., events occurring faster than the used Δt cannot be captured). However, it is worth noting (i) that the quantitative LENS numbers are of little interest, while their comparison, distributions, and the fashion of the LENS timeseries are the key interesting points. Furthermore, (ii) while the microscopic details captured may change with the Δt (Figure S4, left: *e.g.*, Δt = 5ns vs. 50 ns), the analysis remains quite robust on a macroscopic level, and grouping the adjacent microclusters into dynamic macroclusters based on the hierarchical interconnection dendrogram provides the same (coarse-grained) results in both cases (Figure S4: right). While, as in many other types of analyses, a preliminary phase of similar tests is useful to identify the best match between high-resolution and robustness/relevance in the obtained results, the LENS analyses reported herein demonstrated a considerable robustness in the obtained global results.

Figure 2e,f illustrates the main outcomes of the global statistical analysis explained in the previous paragraph. The collected data, D_i^T, are organized into a count matrix where the single entry i,j defines the total number of neighboring events between lipids i and j (Figure 2e). Although such statistical analysis is unrelated to the temporal sequence of the C_i^ts, the global D^T matrix allows distinguishing the propensity of a certain lipid to be, *e.g.*, persistently surrounded by the same neighbors or by a population in continuous exchange (reshuffling) during the simulation. After hierarchical clustering (HC) of the D^T matrix data (see Methods for details), four main dynamic domains are identified (Figure 2e, right): in green, light-blue, orange, purple. Lipid molecules characterized by a similar distribution of neighbor contacts in the D^T matrix are classified in the same dynamics domain. For a more quantitative investigation, we also define a *Variability* (*V*) parameter by estimating the standard deviation of the D_i^T: the broader is the distribution of the neighbor IDs, the higher is the *Variability* (see Methods for details). The analysis shows that the green and light-blue domains are identically highly dynamic, while the orange and purple clusters, similar to each other from a dynamical standpoint, are ~ 4 times more static (Figure 2f, left). Note that, while having the same variability and local-shuffling dynamics, the two green/light-blue (and orange/purple) clusters are identified in this analysis as separate environments. In fact, since the bilayer model replicated on the *xy* through periodic boundary conditions, the **DIPC** and **DPPC** lipids belonging to the upper leaflet do not get in contact with those in the bottom one (their D_i^T distributions do not overlap). The histograms in Figure 2f (right) reveal that the green and blue clusters correspond to red **DIPC** lipids, while the orange and purple domains correspond to the blue **DPPC** molecules. This is consistent with the experimental evidence,(62) showing that the **DIPC** lipids form a liquid phase segregating from gel-phase **DPPC** molecules at the simulation temperature. It is worth noting how the macroclusters obtained with the global statistical analysis (Figure 2e,f) correspond in these case to those obtained *via* LENS-based clustering. As anticipated, such correspondence occurs only in those systems composed of "statistically dominant" different dynamic domains, as in this case, where a liquid and a fluid phase coexist in the bilayer system. In the next sections, we will also discuss cases where LENS detects fluctuations that get lost and cannot be tracked *via* such global/average analyses, since they are not statistically relevant.

To test the generality of our approach, we also tested the same analysis on a CG-MD simulation trajectory of a bi-component micelle model (Supplementary Figure S2) made of n-stearoyl L-histidine (**H**) and p-nitrophenyl ester of n-stearoyl L-phenylalanine self-assembling surfactant molecules (see Methods for details).(60) Supplementary Figures S2a-d show how both LENS and the corresponding time-independent *Variability* analyses identify two distinct dynamic domains: a "donut-like" region of **H** surfactants (red) and two separated, flatter circular sections of **F-NP** surfactants (in blue). Similarly to the bi-component lipid bilayer case discussed above, the dynamics of such bi-component micellar assembly appears being thus characterized by different statistically-relevant dynamic domains.

Into phase transitions & dynamic phases coexistence. We also tested the efficiency of LENS in characterizing phase transitions as well as the dynamic coexistence between different phases. To this end, we discuss two different example systems: (i) a (soft) **DPPC** lipid bilayer system undergoing gel-to-liquid transition with increasing temperature, and (ii) a simulation box where crystalline ice and liquid water coexist in correspondence of the melting/solidification temperature.

For case (i), we analyze 1001 consecutive snapshots taken along 1 µs of CG-MD simulations (Δt = 1 ns) of a lipid bilayer model composed of 1152 self-assembled **DPPC** lipids parametrized with the Martini force field (63) at three distinct temperatures: 273 K, 293 K, and 323 K (see Methods for details).(58) It is known that **DPPC** lipid bilayers have a transition temperature gel-to-liquid of $\sim$ 315 K.(66) However, detecting in a robust manner such gel-liquid phases is not straightforward and typically requires sophisticated analysis approaches that are not always trivial to handle.(58, 67) After reducing the number of clusters detected by KMeans (Supplementary Figure S6), LENS identifies two main phases dominating the **DPPC** bilayer at T = 293 K (Figure 3a): the $\delta_i(t)$ data indicates that while the largest part of lipids show a reduced local reshuffling of neighbors over time, a non-negligible portion of them is more dynamic. As shown in Figure 3a (right), two phases coexist at T = 293 K: $\sim 8\%$ of **DPPC** lipids are found in the red phase, which starts nucleating into the blue one ($\sim 92\%$) - see also Supplementary Movie S1. The transition probability between the two phases is also detected and reported on the black arrows. By using the same setup that detected the gel/liquid separation at 293 K, LENS-based clustering identifies two dominating phases in the **DPPC** bilayer at T = 273 K and T = 323 K, respectively: a cyan domain with lower δ_i *vs.* a red environment with higher δ_i, respectively (Figure 3b). Global statistical analysis summarized in Figure 3c by the *Variability* of D_i^T distributions reveals that the dynamic reshuffling of lipids is considerably reduced in the cyan domain compared to the red one ($\sim 2-6$ times). This indicates that the lipids into the cyan cluster most probably correspond to the gel phase, while the lipids in the red environment behave as a liquid phase, as also evident in the red disordered lipid tails compared with the

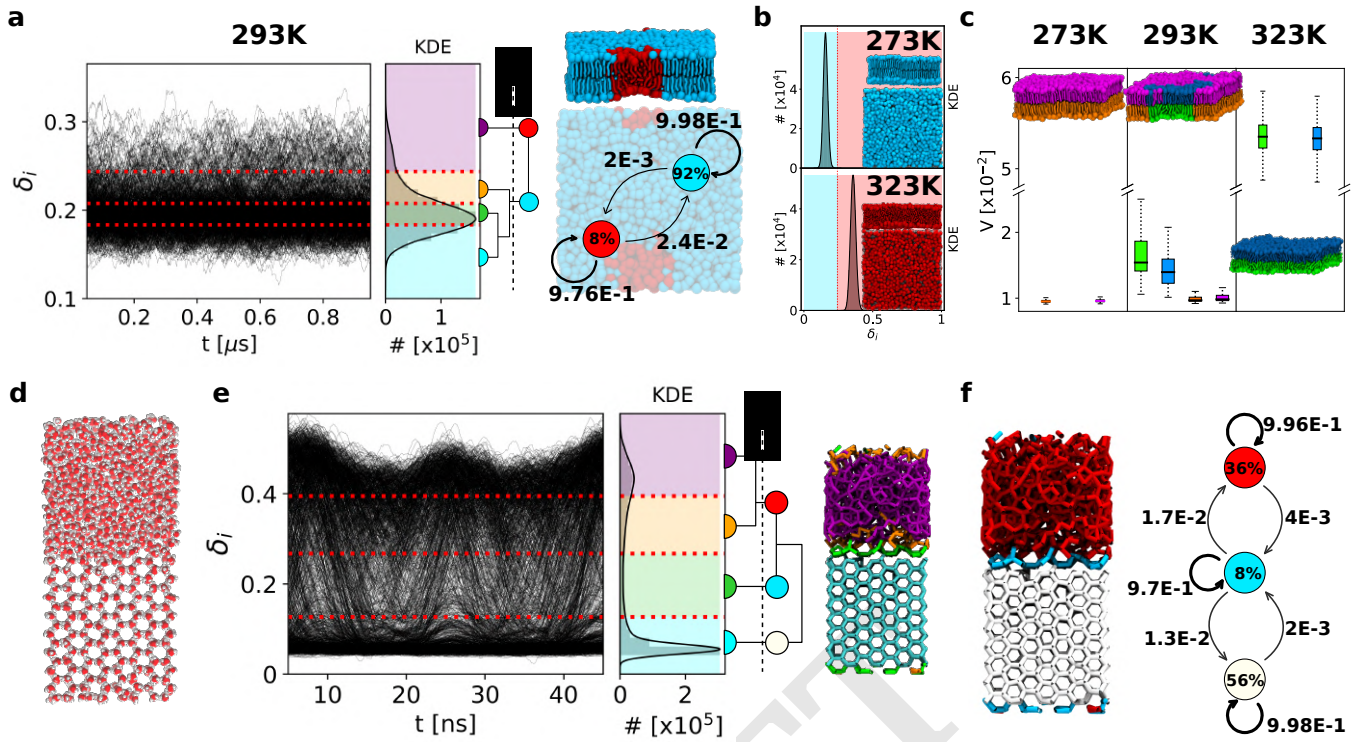

Fig. 3. LENS analysis of multi-phases coexistence. (a) LENS analysis for **DPPC** lipid bilayer in coexistence conditions at $T = 293$ K: time-series of LENS signals, $\delta_i(t)$, with the KDE of LENS distribution, and the interconnection dendrogram identifying two macroclusters in cyan and red (left). MD snapshot of a **DPPC** lipid bilayer colored according to the two main LENS macroclusters (top-right) and related dynamic interconversion diagram (bottom-right). (b) LENS analysis, detecting phase transition at $T = 273$ K (gel) and $T = 323$ K (liquid) for a **DPPC** lipid bilayer. (c) Global statistical neighborhood analysis of the **DPPC** lipid bilayer across a phase transition: at $T = 273$ K the bilayer is in gel-state (low variability V), at $T = 323$ K it is in the liquid-state (high), while two domains (gel and fluid) are detected at $T = 293$ K. (d) **Ice/water** coexistence in an MD simulation (using the TIP4P/Ice water model at 268 K(68)): Oxygen atoms in red and Hydrogen atoms in white. (e) LENS analysis of ice-water coexistence: time-series of LENS signals ($\delta_i(t)$: left) with the KDE of the LENS distribution, and the HC interconnection dendrogram-based clustering (center). The four initially-detected LENS microclusters, represented in different colors in the MD snapshot (right), are merged *via* HC into three main dynamic environments/clusters. (f) Left: MD snapshot showing the three main LENS macroclusters, which identify the liquid phase (in red), the ice phase (in white), and the ice-liquid interface region (in cyan). Right: dynamic interconversion diagram showing how water molecules undergo dynamic transitions from ice-to-liquid and *vice versa*, passing through the ice-liquid interface in such conditions. Note that the sub-units within each considered system are illustrated coherently to the color code of the belonging cluster.

more extended/ordered cyan ones (see the snapshot in Figure 3a). These data thus demonstrate how LENS can blindly distinguish between gel (cyan) and liquid (red) lipid phases and efficiently detect their nucleation and transitions across temperature variations. Furthermore, a 2D Voronoi analysis is found essentially inefficient compared to LENS in detecting the nucleation of small liquid domains and their coexistence within a dominant gel phase in a **DPPC** bilayer at $T = 293$ K (see Supplementary Figure S16). This shows how LENS, despite being a general descriptor, thus not optimized for any system in particular, may perform at least as well, and even better for such soft dynamical systems than ad hoc tailored analyses which typically assume a considerable a priori knowledge of the analyzed systems and are also little transferable to different systems.

For case (ii), we analyze 500 consecutive frames taken every $\Delta t = 0.1$ ns along 50 ns of MD simulation at $T = 268$ K of a periodic box containing 2048 water molecules in total, 1024 of which are in the solid state and arranged in a typical hexagonal ice crystal configuration, while the other 1024, segregated from the first ones, are in the liquid phase (Figure 3d). Shown in Figure 3e, the LENS signals for all water molecules ($\delta_i(t)$ data) clearly demonstrate the presence of two main phases coexisting: one corresponding to low δ_i values (more static behavior), while the second one characterized by higher δ_i values (more dynamic). HC clustering on the dendrogram reduces the number of clusters (Supplementary Figure S7a), identifying three main dynamic phases (Figure 3e): the ice phase (in white), the liquid phase (in red), and the water-ice interface (in cyan). The interconversion diagram of Figure 3f (right) reveals how the ice and liquid phases exchange molecules through such interface cyan region. We underline how such a neat classification is typically non-trivial to be attained *via* sophisticated abstract structural descriptors such as, *e.g.*, SOAP, (69–71) and typical pattern recognition algorithms. On the other hand, with LENS the detection of different dynamic environments emerges in a straightforward manner and simply by tracking differences in the local reshuffling of the individual water molecules.

As additional tests, we have also carried out a systematic comparison between the information that can be inferred *via* our LENS-based analyses *vs.* state-of-the-art benchmark analyses for the ice/water system by using the dynamical propensity (DP) descriptor (see Figure S19). (72) The characterization obtained *via* such DP analysis is found similar to those attained via the average KDE LENS distributions of Figure 3e or *via* our V parameter. This demonstrates how LENS can work at least as well as state-of-the-art DP analysis for such

systems. Nonetheless, it is worth noting that our LENS analysis also retains richer information than those evincible from such averaged analyses. Indeed, from dynamical propensity (DP), KDE LENS distributions, V parameter analyses one can only extract those dynamic domains which are statistically relevant along the sampled trajectory (*e.g.*, ice in equilibrium with water, similar size gel-liquid segregated lipid domains, etc.), while hiding any information about the time–evolution of the contact data. This is a limit, *e.g.*, in the case of out of equilibrium trajectories – where the obtained distribution does not provide any information on the direction of the evolution of the system –, or in the case of sparse/rare local events occurring in the trajectory of the units, which get lost in such averaged analyses due to their negligible statistical weight. While the ensemble average adopted for such analyses may prevent the detection of local (sparse, rare) events, these are instead explicitly captured by the raw LENS time-series data (*e.g.*, Figure 3e, left). The LENS analysis reported herein can be thus considered at least as powerful as, *e.g.*, a DP analysis and, by definition, even more powerful, as it retains complete information of all the microscopic events that can be captured along the trajectory (compatibly with the time-resolution Δt of the analysis).

Into discrete solid-like dynamics. As completely different test cases, we also tested LENS on systems with solid-like dynamics. In particular, we focused on metal surfaces. While metallic crystals are typically considered hard-matter, it is known that they may possess a non-trivial atomic dynamics even well below the melting temperature.(5, 18, 19) In particular, we consider two Cu FCC surfaces **Cu(210)** and **Cu(211)**, having a strikingly different dynamics.

We use a 150 ns long atomistic MD trajectory of a **Cu(210)** composed of 2304 Cu atoms at $T = 700$ K (Figure 4a) conducted with a dynamically-accurate deep-potential neural network force field trained on DFT calculations.(5) We analyze with LENS 502 consecutive frames taken every $\Delta t = 0.3$ ns along the MD simulation (see Methods section for details). The LENS signals indicate that the large part of the atoms of this surface is substantially static, while a considerable fraction of the atoms is more dynamic. The LENS-based clustering, applied coherently with the protocol described above, detects three main dynamic domains (Figure 4b, right), corresponding essentially to dynamic surface domains (in red), more static surface and sub-surface domains (cyan), and the crystalline bulk of **Cu(210)** (gray), containing respectively $\sim$ 8%, $\sim$ 18%, and $\sim$ 74% of the Cu atoms in the model system (Figure 4c: cluster populations in the colored circles). The dynamic interconversion plot in Figure 4c reports the probabilities (in $\Delta t = 0.3$ ns) for atomic exchange between the three main LENS environments, revealing a continuous dynamic exchange of atoms between surface, sub-surface and bulk in the nanosecond-scale consistent with what recently demonstrated.(5)

As a second case, we analyze a **Cu(211)** surface composed of 2400 atoms at 600 K (Figure 4d). We analyze with LENS 502 consecutive frames taken every $\Delta t = 0.3$ ns along an MD simulation performed with the same deep-potential force field of the previous case (see Methods for details).(5)

Such **Cu(211)** surface has completely different dynamics than the **Cu(210)** one. In this case, the time-series $\delta_i(t)$ data provide clear evidence of strikingly non-uniform dynamics (Figure 4e). In the **Cu(210)** simulation at 700 K LENS shows a "fluid-like" atomic surface dynamics. Conversely, in the **Cu(211)** surface the LENS-based clustering shows that most of this surface is solid/static (Figure 4f: $\sim$ 99.8% of atoms in the gray cluster and have a low δ_i), while sparse atoms (Figure 4f: $\sim$ 0.1-0.2% in the orange and violet clusters) diffuse and move fast on the surface (large δ_i LENS signal). Such sparse atoms dynamically emerge, diffuse, and reabsorb on the **Cu(211)** surface in a dynamic fashion: in total, we observe $\sim$ 200 gray-to-orange transitions over $\sim$ 500 sampled frames (transition frequency of one event every 750 ps of simulation). The transition matrix in Figure 4f describes the kinetic hierarchy between the different static/dynamic LENS states, revealing in orange those atoms in the surface edges which are prone to move (Figure 4f, bottom: MD snapshot), while in violet are the atoms moving at high-speed on the surface after leaving the orange edge defects (see also Supplementary Movie S2).

In this last case, LENS reveals a strikingly non-uniform dynamics governed by local rare fluctuations, which are typically poorly captured by average-based analyses such as, *e.g.*, pattern recognition approaches, or the global statistical analysis reported for the previous cases (Supplementary Figure S12a).(5, 16) This underlines the efficiency of a local time-lapse LENS analysis to detect such rare fluctuations, which has been challenged further with other prototypical case studies as discussed below.

LENS detection & tracking of local fluctuations. We tested LENS on other molecular systems whose dynamics is dominated by local fluctuations.

First, we focus on a 309-atoms icosahedral Gold nanoparticle (Figure 5a: **Au-NP**). It is known that such metal NPs may possess non-trivial dynamics even at room temperature.(16) We analyze 1000 consecutive frames taken every $\Delta t = 1$ ns along 1 µs of MD simulation at 200 K of temperature (all atoms are thermalized to guarantee that the temperature is globally constant in the **Au-NP** – see Methods for details).(16) At $T = 200$ K, the atomic motion is reduced and the ideal icosahedral architecture of the **Au-NP** is consequently more stabilized than at, *e.g.*, room temperature.(16) Nonetheless, after $\sim$ 180 ns of MD simulation the LENS signal rapidly increases from $\sim$ 0.02 to $\sim$ 0.18 (Figure 5b: $\delta_i(t)$). HC clustering of the dendrogram of Figure 5b provides four main LENS dynamic domains (in gray, cyan, orange, and violet, going from the lowest to the highest δ_i values). Focusing on one **Au-NP** vertex (Figure 5c, bottom: in the **Au-NP** center), its surrounding area, initially static (in gray in the 1st MD snapshot on the left), this vertex becomes suddenly more dynamic (2nd MD snapshot: in orange) and, as a dynamic wave, this area turns then violet (3rd snapshot). Between the 2nd and 3rd snapshots from the left in Figure 5c (bottom), LENS detects a local event well-known in icosahedral Au NPs: one vertex (having five-neighbors in an ideal icosahedron) penetrates inside the NP surface generating a concave "rosette" (having six-neighbors – in violet).(73) Such local transition/fluctuation breaks-down the **Au-NP** symmetry, generating a dynamic region that then coexists with a more static area, in gray (see also Supplementary Movie S3). The data in Figure 5c (top) report the transition probabilities between the detected LENS dynamics domains. This case demonstrates how rare local fluctuations may generate larger collective rearrangements and

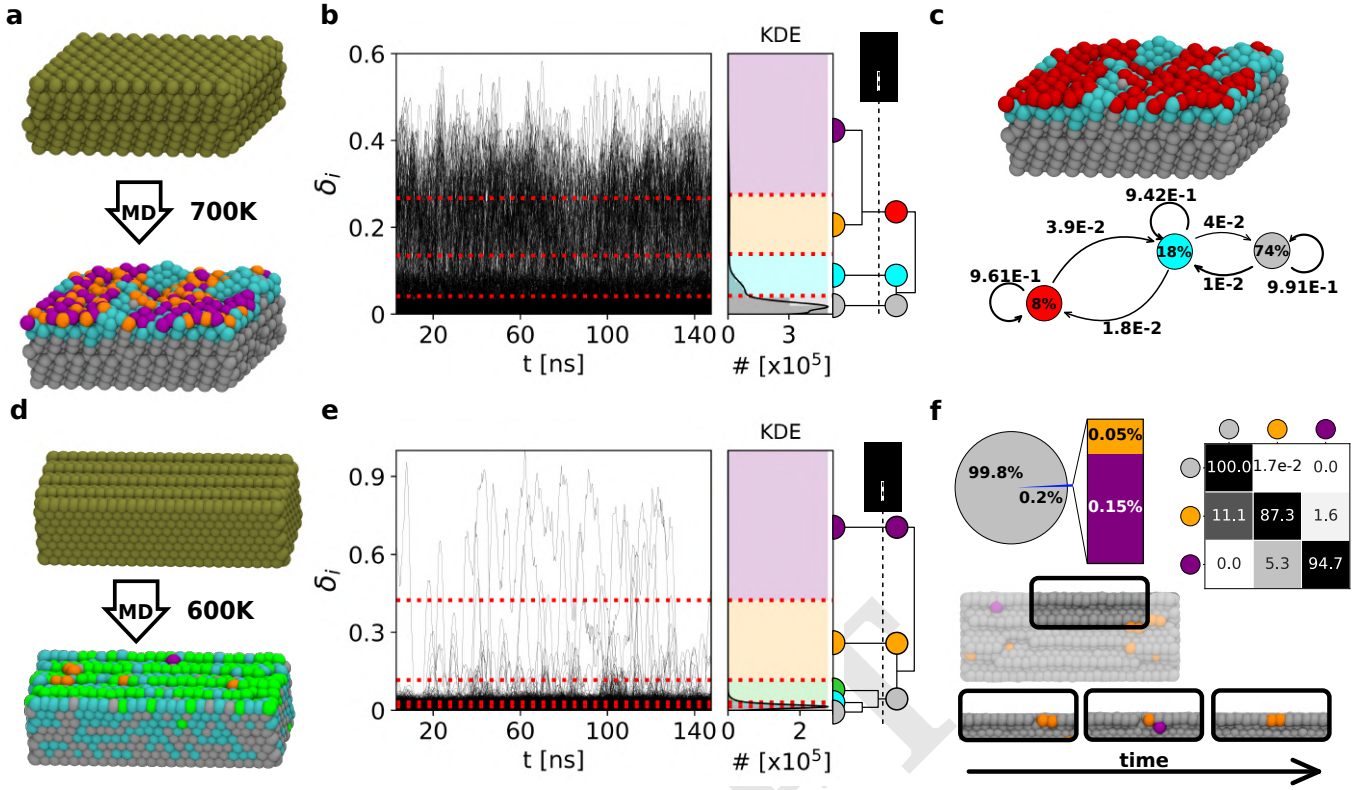

Fig. 4. LENS Analysis of dynamic metal (Cu) surfaces. (a) MD snapshots of an ideal **Cu(210)** surface (top: 0 K) and of the same surface at $T = 700$ K (bottom): atoms colored according to their LENS-detected dynamic environments of belonging. (b) Time-series of LENS signals, $\delta_i(t)$, with the KDE of LENS distribution, and interconnection dendrogram. Four dynamic domains are first identified by KMeans and then merged into three clusters via HC. (c) MD snapshot of **Cu(210)** stable bulk in gray, surface in cyan, and dynamic surface spots in red (top). Dynamic interconversion diagram reports the transition probabilities on the arrows and the cluster composition percentages within the colored circles (bottom). (d) MD snapshots of **Cu(211)** ideal (top) and equilibrated surface at $T = 600$ K (bottom) colored according to LENS clusters. (e) Time-series of LENS signals, $\delta_i(t)$, with the KDE of LENS distribution, and interconnection dendrogram. Five clusters are detected by the LENS-based analysis and merged into three macroclusters. (f) Pie-chart of the clusters compositions and transition probability matrix of the clusters (top). The merged clusters define the surface characterization: the bulk (silver domain), and dynamic atoms which move on the surface breaking/reconstructing rows (orange and purple). Representative MD snapshots showing the surface reconstructions over time are shown on the bottom. Note that the sub-units within each considered system are illustrated coherently to the color code of the belonging cluster.

the efficiency of LENS in detecting them.

As additional tests, we have also carried out different control analyses using the Steinhardt (74) order parameters or SOAP (43) descriptors on the **Cu(211)** surface at $T = 600$K and on the **Au-NP** at 200K (see Supplementary Figure S17 and Figure S18). These comparisons demonstrate how, while such sophisticated descriptors may preserve a structurally rich characterization of the systems, (5, 16) the emergence of rare fluctuations or local transitions are typically overlooked in such structure-based pattern-recognition analyses (see Figure S17). In particular, the few atoms running sensibly faster than all other ones on the **Cu(211)** surface at 600K, are efficiently captured by LENS (see Figure 4*f* and in Movie S2 with clusters in orange and purple), but they get lost in such analyses due to their negligible statistical weight. In similar way, the clear evidence provided in Figure 5 that half **Au-NP** surface becomes highly dynamic following to the conversion of one vertex into a rosette, while the other half remains crystalline-like, is difficult to attain via averaging the dynamic transitions between the many atomic surface environments identified by structural-based analyses (16) (see also Figure S18). In this sense, LENS is found complementary to such structural analyses, providing details that cannot be easily captured by them and that are fundamental to understand the dynamical properties of such systems.

Local transitions/fluctuations are not exclusive of crystalline-like materials, but may be present also in soft systems. We use LENS to analyze a water-soluble 1,3,5-benzenetricarboxamides (**BTA**) supramolecular polymer composed of monomers that self-assemble directionally *via* $\pi - \pi$ stacking and hydrogen-bonding interactions (Figure 5d).(75, 76) It has been demonstrated how these supramolecular fibers possess interesting dynamics due to defects that continuously form and annihilate in a dynamic way in the monomer stack.(6, 7, 50) In this case, we analyze 20001 consecutive frames taken every $\Delta t = 1$ ns along 20 µs of CG-MD simulation at room temperature (see Methods for details).(6, 7) Recently, unsupervised clustering of SOAP data extracted from the MD trajectories of such **BTA**-fibers allowed the unbiased detection of the fiber's defects. However, unveiling *a posteriori* from such structural data the dynamics of these defects and of monomers' diffusion between them is non-trivial.(7, 50) Nonetheless, the time-series $\delta_i(t)$ data in Figure 5e clearly show how the dynamics of such fibers is strongly controlled by sharp local fluctuations that are well captured by LENS. HC clustering of the LENS data distinguishes well the interior of the fiber as a more static environment (Figures 5e,f: gray cluster), the defects along the fiber as slightly more

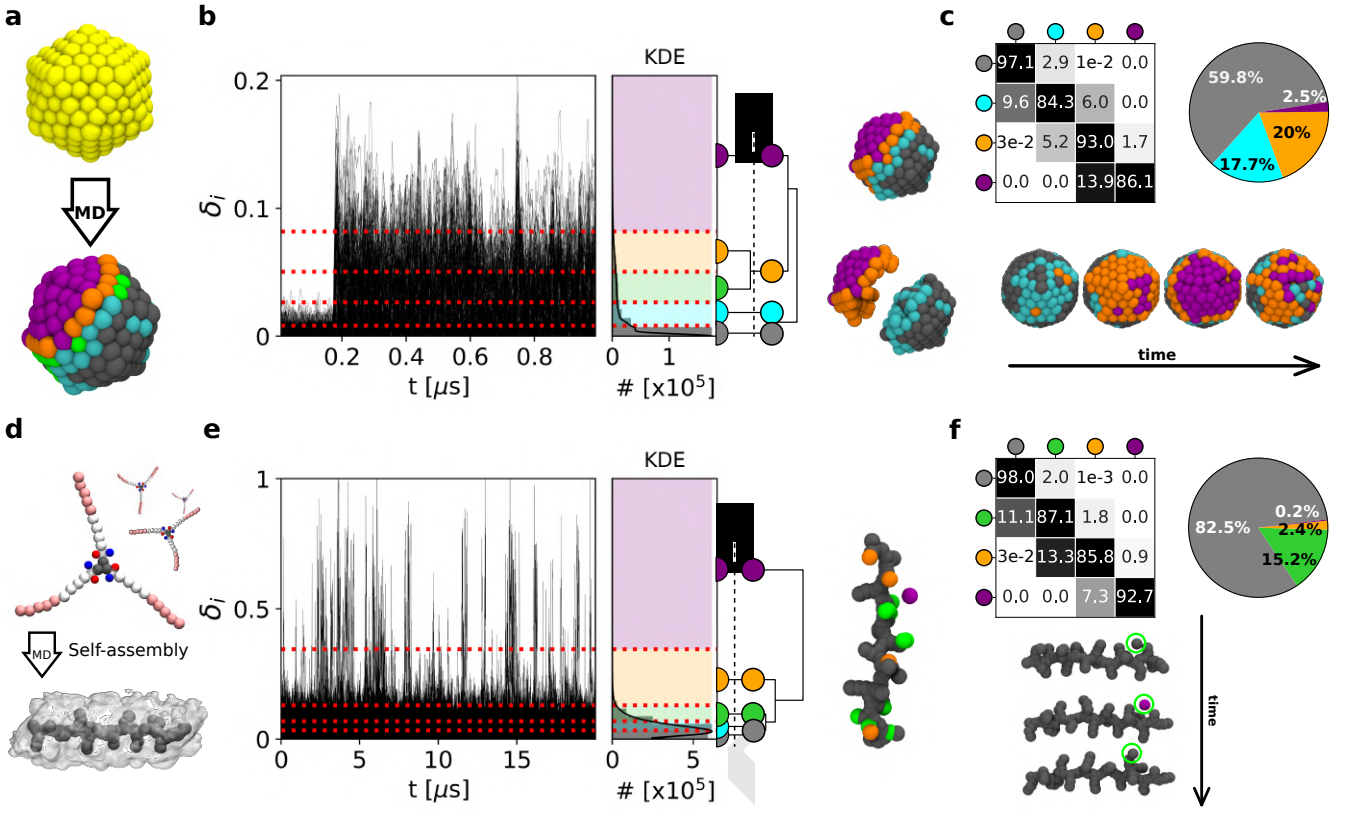

Fig. 5. LENS analysis for discrete-like dynamics and local fluctuations. (a) Ideal icosahedral **Au-NP** (top: at 0 K) and at 200 K (bottom): atoms colored based on their LENS clusters of belonging. (b) LENS analysis: time-series $\delta_i(t)$ signals (left), with the KDE of LENS distribution and interconnection dendrogram (center). Right: The four HC resulting LENS clusters show a clear characterization of the **Au-NP**: one ordered/static region (gray), one intermediate ordered/dynamic domain (cyan), and a mobile area (in orange and purple). (c) Transition probability matrix and cluster composition pie chart (top). Bottom: example of local symmetry breakage in the icosahedral **Au-NP**. After ~ 180 ns of MD simulation, between the 2nd and 3rd snapshots from the left, one vertex (in orange: natively having 5 neighbor atoms) disappears and is replaced by a rosette (in violet: having 6 neighbor atoms). (d) **BTA** monomers (top) and an equilibrated model of a **BTA** self-assembled fiber (bottom). (d) LENS analysis: time-series $\delta_i(t)$ data (left), with related KDE of LENS distribution and interconnection dendrogram (center). Right: detected LENS clusters, corresponding to the bulk (in gray) and the defect domains in the **BTA** fiber (green and orange), and to the monomers diffusing from defect to defect on the fiber surface (in purple). (f) Transition probability matrix and cluster population pie-chart (top). Bottom: example of monomer motion (in the green circle) between defects on the fiber surface, consistent with what the processes of monomer reshuffling demonstrated recently for these fibers.(6, 7, 50) Note that the sub-units within each considered system are illustrated coherently to the color code of the belonging cluster.

dynamic (green and orange), and also the monomers diffusing on the fiber surface (in violet).(6, 7) The transition matrix and pie-chart of Figure 5f show how the gray, green, and orange clusters include the majority of the **BTA**-monomers. On the other hand, sparse monomers ($\sim 0.2\%$) belonging to the violet cluster undergo sharp transitions and instantaneous reshuffling of their local neighbors. These are the monomers that are diffusing defect-to-defect on the fiber surface, which provides a picture of the internal dynamics of such complex **BTA** fibers in optimal agreement with previous studies.(6, 7, 32, 50)

Also in these cases (as in the **Cu(211)** surface of Figure 4d-f), LENS is found efficient in detecting and tracking local fluctuations that play a dominant role in the dynamics of the entire system. It is worth noting how in all such cases a time-independent (pattern recognition-based) statistical analysis of neighbors variability is inefficient to outline such non-uniform dynamics, due to the low statistical weight of the local events occurring in these systems (see also Supplementary Figure S12).

Discussion

Many molecular systems are controlled by local fluctuations that are often difficult to detect and typically lost in average-based analyses. Here we present a new general descriptor designed to track local fluctuations in complex dynamic systems, named Local Environments and Neighbors Shuffling (LENS). Different from many descriptors, LENS is based on the concept of neighbor identities (IDs) instead of, *e.g.*, molecular/atomic species. At each sampled time-frame along a trajectory, our analysis builds a string listing the neighbor IDs surrounding each particle i in the system. Within the time-interval between consecutive time-frames, LENS measures the variations in the neighbor IDs in terms of addition, subtraction, or reshuffling of neighbors (Figure 1). Large time-lapse variations in the local neighborhood provide strong LENS signals, while weak LENS signals indicate reduced dynamics in the local environment surrounding a given particle i.

We tested LENS in a number of systems with strikingly different internal dynamics. Shown in Figure 2, LENS reveals that a bicomponent lipid bilayer is characterized by surface patches, with different molecular reshuffling dynamics, which correspond to the segregation of the lipid species into two do-

mains. In Figure 3, we demonstrate how our time-series LENS analysis detects efficiently phase transitions and coexistence of different phases: *e.g.*, in a **DPPC** lipid bilayer undergoing gel-to-liquid transition increasing the temperature from 273 K to 323 K, or in a liquid water-ice system at freezing/melting temperature.

When a system is characterized by statistically-dominant dynamic domains, the time-dependent LENS and global (time-independent) statistical analyses correlate (Figure 2 and Figures 3a-c). Conversely, system dynamics dominated by rare local fluctuations are poorly described by global statistical analyses (Supplementary Figure S12). In the **Cu(211)** surface (Figure 4d-f), for example, a global statistical analysis based on a pattern recognition approach identifies only one domain, as reported in Supplementary Figure S12a, meaning that the sparse atoms diffusing fast on the metal surface are not statistically relevant and are statistically-lost in such analyses. Rare local transitions are not captured by a global time-independent analysis even in the systems of Figure 5. This is not necessarily an exclusive problem of time-independent analyses conducted with this specific descriptor: also other descriptors such as, *e.g.*, SOAP, coordination number, etc., are in fact efficient as far as they are used to detect statistically-relevant dynamic/structural populations and patterns. Nonetheless, the results of Figures 4d-f and 5 demonstrate how a local time-dependent LENS analysis is efficient in detecting and tracking such local fluctuations, and in this sense appears as more general, complete, and robust than an average time-independent investigation. In addition, while average-based and global pattern recognition analyses work typically well when one knows what to search, this is less the case for LENS. The LENS analysis in fact only requires knowing the IDs of the interacting particles and having a sufficiently sampled trajectory. This is fundamental in most practical cases where the nature of a system is not known *a priori*. In principle, for ensuring a sufficient sampling of the events captured from the analyzed trajectories, it would be desirable to use a sampling Δt small enough to capture the interesting fluctuations/transitions and to have at disposal a sufficiently long trajectory to ensure that statistically relevant information on given events can be effectively attained. It would be ideal to analyze a very long trajectory using a very tight sampling (small Δt), however, in most practical cases, this is limited by, *e.g.*, the complexity of the system, the available computational power, and by the cost of the analysis (which could produce large dataset difficult to handle/analyze and full of irrelevant information and noise). Like in the majority of analyses, a preliminary test phase is thus required to optimize the resolution/cost of the LENS analysis. For example, in our cases our preliminary tests demonstrated that a sampling time (Δt) in the range of 1-10 ns produced robust insightful results, *e.g.*, in the case of the CG simulations of lipids, while a smaller time-step in the range of 0.1-1 ns was found best suited for, e.g., the AA simulations and solid-state systems studied herein (water/ice, Cu surface, Au-NP). The (temporal) resolution of the analysis (Δt) can be adjusted/optimized to focus on specific events of interest. The raw time series LENS data (as well as the transition matrices recomputed from them reported in the Figures) provide information on the statistical confidence in the identification of the different dynamical domains populating the various systems and on the observation of the various transitions/fluctuations between them.

To test the robustness and efficiency of the LENS descriptor, we have carried out a systematic comparison between LENS and existing reference techniques, typically used as a benchmark for the various systems studied herein (Voronoi (65), Steinhardt (74), Mean Square Displacement, Dynamical Propensity (DP) (72) analyses). These additional tests show how LENS works at least as well as such analyses, which are considered state-of-the-art for the various testes systems, and even better (see Figures S15-S19). At the same time, a strong advantage of LENS is its generality. Differently from most of such benchmark analysis approach, LENS is not tailored ad hoc on a specific system and does not require prior knowledge of the studied systems. LENS is thus in principle transferable and well suited to reveal the dynamical features of a variety of systems (as demonstrated by the diverse test systems used herein). Our tests also show how, while such benchmark techniques can capture structurally rich information, they may be inefficient, *e.g.*, in capturing local and rare dynamical events/fluctuations, key for the unveil the system properties, and which are instead well described by LENS.

LENS has also some intrinsic limitations. Based on its definition, if in Δt the neighbors do not change (same IDs) but move remaining in the r_{cut} sphere (local structural rearrangement of the neighborhood), LENS provides no signal. This is opposed to descriptors such as, *e.g.*, SOAP that – being permutationally invariant – provide *vice versa* a signal in case of local rearrangements, but no signal in case of a switching of IDs (keeping the same structural displacement). This makes LENS best suited to measure local dynamicity rather than local structural variations, which is nonetheless key in many complex systems where dynamics plays a major role. At the same time, one key advantage of LENS is its abstract definition. This makes it well suited to analyze a variety of trajectories of systems for which the identities of the moving units are known and, in principle, not necessarily restricted to molecular ones.

Materials and Methods

MD simulations. All data concerning the molecular models and the MD trajectories analyzed herein are available at: https://github.com/GMPavanLab/LENS (this link will be replaced with a definitive Zenodo archive upon acceptance of the final version of this paper).

The **DIPC**/**DPPC** lipid bilayer (Figure 2) is simulated using the Martini2.2 force field.(63) A binary mixture of dipalmitoyl-phosphat-idylcholine (**DPPC**) and dilinoleoyl-phosphatidyl-choline (**DIPC**), with 2:3 molar ratio, is used to model the coexistence of liquid-crystalline and gel phases into such self-assembled bilayer. To get the separation of the bilayer into domains of coexisting phases, the mixture was simulated at $T = 280$ K. The initial configuration of the binary lipid mixture in water is generated using *insane* (77) with the specified box dimensions (18 x 18 x 11 nm). The bilayer system is composed of 1150 lipids, consisting of 2:3 **DIPC**:**DPPC** on each leaflet, and 17987 (W) water molecules. To prevent water crystallization ($T < 290$ K in Martini),(63) $\sim 5\%$ of regular water particles are substituted by the anti-freezing water particles. For non-bonded interactions, a reaction-field electrostatics algorithm is used with a Coulomb cutoff of $r_c = 1.1$ nm and a dielectric constant of 15. The cutoff for Lennard-Jones interactions is set to $r_{LJ} = 1.1$ nm. The timestep used during the MD simulation is $\delta t = 20$ fs. The system is preliminarily minimized and equilibrated for $t = 100$ ns. A production run is then performed for $t = 15$ µs, and the data acquisition is performed every 1 ns. The solvent and membrane are coupled separately using a v-rescale thermostat with a relaxation time of $t = 1.0$ ps. During the equilibration, the

pressure is maintained at $p = 1$ bar using the Berendsen barostat with the semi-isotropic coupling scheme, a time constant of $\tau_p = 4$ ps, and compressibility $c = 3 * 10^{-4}$ bar^{-1}. During the production, the Parrinello-Rahman barostat is used, with a time constant of $\tau_p = 12$ ps. An equilibrium part of the trajectory is analyzed (the last 10 µs) every $\Delta t = 10$ ns (1001 sampled frames).

The bicomponent **F-NP**/**H** micelle (Supplementary Figure S2) was simulated at $T = 300$ K in explicit water *via* Martini2.2 (63) scheme (see reference (60) for further details). The system is a binary mixture of p-nitrophenyl ester of n-stearoyl L-phenylalanine (**F-NP**) and n-stearoyl L-histidine (**H**) with 1:1 molar ratio ($N_{\mathbf{F\text{-}NP}} = 100$ and $N_{\mathbf{H}} = 100$). The initial configuration consists of $N_{\mathbf{F\text{-}NP}} = 100$ and $N_{\mathbf{H}} = 100$ randomly dispersed surfactants, which assemble into a single micelle within a 10 µs long MD simulation sampled every 1 ns. The last 3 µs of the MD trajectory is considered representative of the equilibrium(60) and used for the analysis – 3001 analyzed frames taken every $\Delta t = 1$ ns along the MD.

All the **DPPC** lipid bilayer trajectories at $T = 293$ K, 273 K and 323 K (Figure 3a-c) are obtained from MD simulations of a bilayer model composed of $N_{DPPC} = 1152$ **DPPC** lipids, simulated and parameterized in explicit water *via* Martini2.2, (63) as reported in reference (58). The equilibrated-phase MD trajectories used for the analyses are in all cases 1 µs. A total of 1001 frames extracted every $\Delta t = 1$ ns along the MD trajectories are used for the analyses.

The atomistic Ice/Water interface model of Figure 3d-f is simulated employing the direct coexistence technique. The **TIP4P**/**Ice** water model(78) is used to model both the solid phase of ice I_h and the phase of liquid water. The direct coexistence technique is based on the idea to put in contact more phases in the same box and at constant pressure. To get the coexistence, the temperature is set at $T = 268$ K (the energy is constant at 268 K and the system melts at 269 K(68)), kept constant using the v-rescale thermostat with a relaxation time of $t = 0.2$ ps. The initial configuration of the ice I_h is obtained using the *Genice* tool proposed by Matsumoto *et al.*(79) generating a hydrogen-disordered lattice with zero net polarization satisfying the Bernal-Fowler rules. To equilibrate the solid lattice, anisotropic *NPT* simulation is carried out using the c-rescale barostat, with a time constant of $\delta t = 20$ ps and compressibility of $9.1 * 10^{-6}$ bar^{-1}. The equilibration lasted 10 ns at ambient pressure (1 atm). The liquid phase is obtained from the same ice I_h solid phase, performing a *NVT* simulation at $T = 400$ K to quickly melt the ice slab. Thus, both the solid and liquid phases are obtained with the same number of molecules (1024) and box dimensions. The liquid phase is then equilibrated at $T = 268$ K for $t = 10$ ns, using the c-rescale barostat in semi-isotropic conditions and compressibility of $c = 4.5 * 10^{-5}$ bar. The two phases are, then, put in contact and equilibrated for $t = 10$ ns using the c-rescale pressure coupling with the water compressibility ($c = 4.5 * 10^{-5}$ bar) at ambient pressure. The production *NPT* ice/water coexistence MD simulation (Figure 3d-f) is performed in semi-isotropic conditions, with the pressure applied only in the direction perpendicular to the ice/water interface. This allows to reproduce the strictly correct ensemble for the liquid-solid equilibrium simulation by the direct coexistence technique. After the equilibration, a production run is performed for $t = 50$ ns, sampled and analyzed every 0.1 ns. All the trajectories analyzed for the systems simulated above are obtained using the GROMACS software.(80)

The atomistic models of the **Cu(210)** and **Cu(211)** surfaces (Figure 4) are composed of $N_{210} = 2304$ and $N_{211} = 2400$ atoms, respectively. The MD simulations are conducted at $T = 700$ K and at $T = 600$ K respectively for the two example surfaces. Deep-potential MD simulations of both Cu surfaces are conducted with the LAMMPS software(81) using a Neural Network potential built using the DeepMD platform,(82) as described in detail in reference (5). The sampled trajectories are 150 ns long. A total of 502 frames are extracted every $\Delta t = 0.3$ ns along the MD trajectories and used for the LENS analyses.

The atomistic model for the icosahedral **Au-NP** is composed of $N_{Au-NP} = 309$ gold atoms (Figure 5a-c). The **Au-NP** model is parametrized according to the Gupta potential, (83) and is simulated for 1 µs of MD at $T = 200$ K using the LAMMPS software(81) as described in detail in reference (16). 1000 frames are extracted every $\Delta t = 1$ ns of the MD trajectory and then used for the analyses.

The coarse-grained **BTA** fiber model is built consistent with the MARTINI force field(63) and optimized as described in detail in references (6, 37). In particular, the fiber model is composed of $N_{BTA} = 80$ **BTA** monomers. A trajectory of 20 µs, obtained with the GROMACS software(80), is then analyzed every $\Delta t = 1$ ns (20001 sampled frames in total).

Pre-processing of the trajectories. All MD trajectories are firstly pre-processed in order to obtain plain `xyz` files keeping only the coordinates of the particles of interest, *i.e.*, considered during the neighborhood's evaluation, as reported in Supplementary Table S1. For example, in the lipid bilayer analyses of Figures 2 and 3a-c we considered only the tan PO4 (MARTINI) beads as representative of the "center" position of each lipid molecule in the systems. For the micelles of Supplementary Figure S2, we used the center of mass of the surfactant heads as the centers for the analysis, for the water/ice system (Figure 3d-f), we considered only the Oxygens of the water molecules, for the metal surfaces and **Au-NP** (Figure 4 and Figure 5a-c) information of each atom was retained, while for the **BTA** fiber, we considered only the center of each monomer core as a reference for the LENS analyses. In all cases, the analysis is then conducted by building at each sampled timestep strings collecting the neighbor IDs of each unit i within a sphere of radius r_{cut} (which is set depending on the system and based on the shape and the minima of the radial distribution functions, $g(r)_m$ – see Supplementary Table S1 and Supplementary Figure S1).

Time-lapse LENS analysis. The instantaneous δ_i parameter for each unit i in each model system is calculated over time along the system's trajectory from the C_i strings containing the IDs of the neighbor units calculated at times t and $t + \Delta t$ as reported in Equation 1. The analysis is then repeated for all units i at all time-intervals Δt sampled along the analyzed trajectories, obtaining the $\delta_i(t)$ plots of Figures 1b,2b,3a,3e,4b,4e,5b and 5e. The δ_i parameter is normalized such that it gives 0 when the local neighborhood does not change and 1 when it changes completely at each Δt. To reduce the noise in each $\delta_i(t)$ signal, we processed them by using a Savitzky–Golay (84) filter (as implemented in the SciPy python package (85)), obtaining smoothed $\langle\delta_i(t)\rangle$ signals. In particular, each $\delta_i(t)$ signal is smoothed using a common polynomial order parameter of $p = 2$ on a time-window of 100 frames for the bicomponent **DIPC/DPPC** lipid bilayer system, the **F-NP/H** micelle, **DPPC** lipid, and for the water/ice interface. A smaller time-window of 20 frames was used for the crystalline **Cu** surfaces, for the gold **Au-NP**, and for the **BTA** systems, which allows to better capture the rapid emergence of rare fluctuations within them. Such setups were considered as the best compromise in the various cases after a preliminary phase in which we tested the reliability and robustness of results by systematically studying the effect of changing the smoothing windows on the results obtained for the various systems (see Supplementary Figure S5, Figure S6, Figure S7). In order to simplify the notation, we refer to the $\langle\delta_i(t)\rangle$ signal as δ_i.

After the noise reduction, the clustering of the δ_i data is performed by means of KMeans algorithm (64) implemented in SciPy python package (85). The KMeans algorithm requires the definition of the number of clusters as an input. The initial number of microclusters is set (as a default choice) as twice the number of peaks/discontinuities in the δ_i data (distributions on the right of Figures 1b,2b, 3a, 3e, 4b, 4e, 5b and 5e), while in case only one peak is detectable in the δ_i distribution, the initial number of microclusters is always set to five). This guarantees that KMeans always detects an excess of starting microclusters, allowing us to start from an excess of dynamical information. After such preliminary step, a transition matrix is built collecting the probabilities for each single identity/sub-unit belonging to a certain specific cluster at time t to remain in that cluster (diagonal entries) or to undergo transition into another one in Δt (off-diagonal matrix entries). Then, the microclusters are merged hierarchically a posteriori into macroclusters based on a concept of direct closest adjacency (*i.e.*, clusters having the smallest distance from each other are merged together). To this end, a *single* link algorithm based on the metrics *correlation* implemented in the HC interconnection dendrograms is used. Specifically, the HC algorithm first computes the distances, according to the selected metrics -*correlation*-, between any couple of rows (clusters) in the transition matrix, then it couples/merges specific rows following the *single* algorithm rational. This implies

that clusters in the transition matrices having, *e.g.*, high diagonal % entries (higher than 50%) are kept as distinct, meaning that within the time resolution of the analysis they are recognized as dynamically distinct environments with good statistical confidence, while clusters with low off-diagonal % entries (*e.g.*, close to or lower than 50%) and high off-diagonal entries % (high probability to undergo transition into another cluster in Δt) are most likely merged together. Such a Hierarchical-clustering (HC) approach is used to relate all microclusters with each other, and to provide the rationale for merging them into the macroclusters reported in our analyses based on their adjacency, thereby obtaining a coarse-grained characterization of the internal dynamics of the studied systems. This is the effect of cutting the HC dendrogram at different levels (see Supplementary Figures S6,S7,S8,S9,S10 and S11).

We note that the results shown herein are obtained *via* such a simple iterative supervised clustering approach, which in the cases we discuss in this work was found simple, effective, and little sensitive to the tuning of clustering parameters (thus satisfactory from the robustness and reproducibility point of view). Nonetheless, we underline that other (*e.g.*, unsupervised) clustering approaches could be used for the purpose, although they do not always provide consistent results with each other, and where the tuning of the setup parameters may be non-trivial.

Global statistical analysis. Average information on the statistically dominant dynamic domains present in the systems can also be obtained from the global dataset of the C_i as described in the text. For each i unit, the numbers of the contacts with the other neighbor IDs along the trajectory (D_i^T, considering all T sampled frames) are collected from the global C_i dataset (see, *e.g.*, Figure 1c). The contacts data are then organized into a contact matrix where the individual entry i, j indicates the total number of neighboring events between the bead i and j in all sampled time-intervals along the analyzed trajectory (Figures 2e and Supplementary Figure S2e).

The data related to each unit i (i.e., to each row of the contact matrix), are centered on the mean and normalized on the standard deviation of the neighboring events. The *Variability* (V) is then defined as the inverse of the standard deviation of the D_i^T values: low standard deviation around a mean value implies that each unit i gets in direct contact with all other IDs along the trajectory, the *Variability* (V) of its neighborhood is thus high. On the other hand, high standard deviation identifies cases where the number of neighbors tend to remain the same along the trajectory and the number of visited neighbor IDs is thus low: this means that the neighborhood of unit i in such cases is rather static, and its *Variability* (V) is low. What is important to note is that, rather than the quantitative V values (which may depend on, e.g., the length of the trajectory, the dynamics of the system, etc.), what is relevant is the comparison between the (V) parameters of the individual units (i: from 1 to n) in the system, and the presence of molecular domains characterized by different V indexes (identifying the presence of different dynamical domains). The matrix is then analyzed *via* Hierarchical Clustering (HC). In particular, the normalized contact data are gathered by means of Ward method (86) with Euclidean metric (both implemented in SciPy python package(85)), and the number of clusters is determined based on the dominant patterns from the sorted matrix (see, *e.g.*, the matrices of Figure 2e and Supplementary Figure S2e, right).

Data availability. Details on the molecular models and on the MD simulations, and additional simulation data are provided in the Supplementary Information. The LENS analysis code, together with complete data on all molecular models used for the simulations and on the simulation parameters (input files, etc.) used in this work are available at https://doi.org/10.5281/zenodo.8013279 (DOI: 10.5281/zenodo.8013279) and at https://github.com/GMPavanLab/LENS.

ACKNOWLEDGMENTS. G.M.P. acknowledges the support received by the European Research Council (ERC) under the European Union's Horizon 2020 research and innovation program (Grant Agreement no. 818776 - DYNAPOL) and by the Swiss National Science Foundation (SNSF Grant IZLIZ2_183336).

1. Y Cho, T Christoff-Tempesta, SJ Kaser, JH Ortony, Dynamics in supramolecular nanomaterials. *Soft Matter* **17**, 5850–5863 (2021).
2. SJ Kaser, T Christoff-Tempesta, LD Uliassi, Y Cho, JH Ortony, Domain-Specific Phase Transitions in a Supramolecular Nanostructure. *J. Am. Chem. Soc.* **144**, 17841–17847 (2022).
3. S Bae, KG Yager, Chain Redistribution Stabilizes Coexistence Phases in Block Copolymer Blends. *ACS Nano* **16**, 17107–17115 (2022).
4. F Baletto, Structural properties of sub-nanometer metallic clusters. *J. Phys. Condens. Matter* **31**, 113001 (2019).
5. M Cioni, et al., Innate dynamics and identity crisis of a metal surface unveiled by machine learning of atomic environments. *J. Chem. Phys* **158**, 124701 (2023).
6. D Bochicchio, M Salvalaglio, GM Pavan, Into the dynamics of a supramolecular polymer at submolecular resolution. *Nat. Commun.* **8**, 147 (2017).
7. P Gasparotto, D Bochicchio, M Ceriotti, GM Pavan, Identifying and tracking defects in dynamic supramolecular polymers. *J. Phys. Chem. B* **124**, 589–599 (2020).
8. T Aida, EW Meijer, SI Stupp, Functional Supramolecular Polymers. *Science* **335**, 813–817 (2012).
9. MJ Webber, EA Appel, EW Meijer, R Langer, Supramolecular biomaterials. *Nat. Mater.* **15**, 13–26 (2016).
10. AJ Savyasachi, et al., Supramolecular Chemistry: A Toolkit for Soft Functional Materials and Organic Particles. *Chem* **3**, 764–811 (2017).
11. L Brunsveld, BJB Folmer, EW Meijer, RP Sijbesma, Supramolecular Polymers. *Chem. Rev.* **101**, 4071–4098 (2001).
12. J Boekhoven, SI Stupp, 25th Anniversary Article: Supramolecular Materials for Regenerative Medicine. *Adv. Mater.* **26**, 1642–1659 (2014).
13. C Lionello, et al., Toward chemotactic supramolecular nanoparticles: from autonomous surface motion following specific chemical gradients to multivalency-controlled disassembly. *ACS nano* **15**, 16149–16161 (2021).
14. MS Spencer, Stable and metastable metal surfaces in heterogeneous catalysis. *Nature* **323**, 685–687 (1986).
15. CS Jayanthi, E Tosatti, L Pietronero, Surface melting of copper. *Phys. Rev. B* **31**, 3456–3459 (1985).
16. D Rapetti, et al., Machine learning of atomic dynamics and statistical surface identities in gold nanoparticles. ChemRxiv [Preprint] (2022) https://chemrxiv.org/engage/chemrxiv/article-details/63642e6aac45c7a2a9a45332.
17. V Yamakov, D Wolf, S Phillpot, A Mukherjee, H Gleiter, Deformation-mechanism map for nanocrystalline metals by molecular-dynamics simulation. *Nat. Mater.* **3**, 43–47 (2004).
18. LA Zepeda-Ruiz, A Stukowski, T Oppelstrup, VV Bulatov, Probing the limits of metal plasticity with molecular dynamics simulations. *Nature* **550**, 492–495 (2017).
19. X Wang, et al., Atomistic processes of surface-diffusion-induced abnormal softening in nanoscale metallic crystals. *Nat. Commun.* **12**, 5237 (2021).
20. R Koch, M Borbonus, O Haase, KH Rieder, Reconstruction behaviour of fcc(110) transition metal surfaces and their vicinals. *Appl. Phys. A* **55**, 417–429 (1992).
21. XQ Wang, Phases of the au(100) surface reconstruction. *Phys. Rev. Lett.* **67**, 3547–3550 (1991).
22. G Antczak, G Ehrlich, *Surface Diffusion: Metals, Metal Atoms, and Clusters.* (Cambridge University Press), (2010).
23. E Gazzarrini, K Rossi, F Baletto, Born to be different: the formation process of Cu nanoparticles tunes the size trend of the activity for CO2 to CH4 conversion. *Nanoscale* **13**, 5857–5867 (2021).
24. AL de Marco, D Bochicchio, A Gardin, G Doni, GM Pavan, Controlling exchange pathways in dynamic supramolecular polymers by controlling defects. *ACS Nano* **15**, 14229–14241 (2021).
25. M Crippa, C Perego, AL de Marco, GM Pavan, Molecular communications in complex systems of dynamic supramolecular polymers. *Nat. Commun.* **13**, 2162 (2022).
26. A Torchi, D Bochicchio, GM Pavan, How the Dynamics of a Supramolecular Polymer Determines Its Dynamic Adaptivity and Stimuli-Responsiveness: Structure–Dynamics–Property Relationships From Coarse-Grained Simulations. *J. Phys. Chem. B* **122**, 4169–4178 (2018).
27. D Bochicchio, S Kwangmettatam, T Kudernac, GM Pavan, How defects control the out-of-equilibrium dissipative evolution of a supramolecular tubule. *ACS nano* **13**, 4322–4334 (2019).
28. L Albertazzi, et al., Probing Exchange Pathways in One-Dimensional Aggregates with Super-Resolution Microscopy. *Science* **344**, 491–495 (2014).
29. D Wang, et al., Structural diversity in three-dimensional self-assembly of nanoplatelets by spherical confinement. *Nat. Commun.* **13**, 6001 (2022).
30. GC Sosso, et al., Unravelling the origins of ice nucleation on organic crystals. *Chem. Sci.* **9**, 8077–8088 (2018).
31. TA Sharp, et al., Machine learning determination of atomic dynamics at grain boundaries. *Proc. Natl. Acad. Sci. U.S.A.* **115**, 10943–10947 (2018).
32. D Bochicchio, GM Pavan, Molecular modelling of supramolecular polymers. *Adv. Phys. X* **3**, 1436408 (2018).
33. PW Frederix, I Patmanidis, SJ Marrink, Molecular simulations of self-assembling bio-inspired supramolecular systems and their connection to experiments. *Chem. Soc. Rev.* **47**, 3470–3489 (2018).
34. OS Lee, V Cho, GC Schatz, Modeling the Self-Assembly of Peptide Amphiphiles into Fibers Using Coarse-Grained Molecular Dynamics. *Nano Lett.* **12**, 4907–4913 (2012).
35. KK Bejagam, S Balasubramanian, Supramolecular Polymerization: A Coarse Grained Molecular Dynamics Study. *J. Phys. Chem. B* **119**, 5738–5746 (2015).
36. C Perego, L Pesce, R Capelli, SJ George, GM Pavan, Multiscale molecular modelling of atp-fueled supramolecular polymerisation and depolymerisation. *ChemSystemsChem* **3**, e2000038 (2021).
37. D Bochicchio, GM Pavan, From Cooperative Self-Assembly to Water-Soluble Supramolecular Polymers Using Coarse-Grained Simulations. *ACS Nano* **11**, 1000–1011 (2017).
38. J Behler, M Parrinello, Generalized neural-network representation of high-dimensional potential-energy surfaces. *Phys. Rev. Lett.* **98**, 146401 (2007).
39. AP Bartók, MC Payne, R Kondor, G Csányi, Gaussian approximation potentials: The accuracy

of quantum mechanics, without the electrons. *Phys. Rev. Lett.* **104**, 136403 (2010).
40. J Behler, Perspective: Machine learning potentials for atomistic simulations. *J. Chem. Phys.* **145**, 170901 (2016).
41. JR Errington, PG Debenedetti, Relationship between structural order and the anomalies of liquid water. *Nature* **409**, 318–321 (2001).
42. K Rossi, L Pavan, Y Soon, F Baletto, The effect of size and composition on structural transitions in monometallic nanoparticles. *Eur. Phys. J. B* **91**, 1–8 (2018).
43. AP Bartók, R Kondor, G Csányi, On representing chemical environments. *Phys. Rev. B* **87**, 184115 (2013).
44. J Behler, Atom-centered symmetry functions for constructing high-dimensional neural network potentials. *J. Chem. Phys.* **134**, 074106 (2011).
45. R Drautz, Atomic cluster expansion for accurate and transferable interatomic potentials. *Phys. Rev. B* **99**, 014104 (2019).
46. F Faber, A Lindmaa, OA von Lilienfeld, R Armiento, Crystal structure representations for machine learning models of formation energies. *Int. J. Quantum Chem.* **115**, 1094–1101 (2015).
47. P Gasparotto, RH Meißner, M Ceriotti, Recognizing local and global structural motifs at the atomic scale. *J. Chem. Theory Comput.* **14**, 486–498 (2018).
48. F Musil, et al., Physics-Inspired Structural Representations for Molecules and Materials. *Chem. Rev.* **121**, 9759–9815 (2021).
49. F Pietrucci, R Martoňák, Systematic comparison of crystalline and amorphous phases: Charting the landscape of water structures and transformations. *J. Chem. Phys.* **142**, 104704 (2015).
50. A Gardin, C Perego, G Doni, GM Pavan, Classifying soft self-assembled materials via unsupervised machine learning of defects. *Commun. Chem.* **5**, 82 (2022).
51. J Andrews, O Gkountouna, E Blaisten-Barojas, Forecasting molecular dynamics energetics of polymers in solution from supervised machine learning. *Chem. Sci.* **13**, 7021 (2022).
52. A Glielmo, et al., Unsupervised Learning Methods for Molecular Simulation Data. *Chem. Rev.* **121**, 9722–9758 (2021).
53. P Gasparotto, M Ceriotti, Recognizing molecular patterns by machine learning: An agnostic structural definition of the hydrogen bond. *J. Chem. Phys.* **141**, 174110 (2014).
54. AP Bartók, et al., Machine learning unifies the modeling of materials and molecules. *Sci. Adv.* **3**, e1701816 (2017).
55. C Chen, W Ye, Y Zuo, C Zheng, SP Ong, Graph Networks as a Universal Machine Learning Framework for Molecules and Crystals. *Chem. Mater.* **31**, 3564–3572 (2019).
56. MB Davies, M Fitzner, A Michaelides, Accurate prediction of ice nucleation from room temperature water. *Proc. Natl. Acad. Sci. U.S.A.* **119**, e2205347119 (2022).
57. F Noé, S Olsson, J Köhler, H Wu, Boltzmann generators: Sampling equilibrium states of many-body systems with deep learning. *Science* **365**, eaaw1147 (2019).
58. R Capelli, A Gardin, C Empereur-Mot, G Doni, GM Pavan, A data-driven dimensionality reduction approach to compare and classify lipid force fields. *J. Phys. Chem. B* **125**, 7785–7796 (2021).
59. C Lionello, C Perego, A Gardin, R Klajn, GM Pavan, Supramolecular semiconductivity through emerging ionic gates in ion–nanoparticle superlattices. *ACS Nano* **17**, 275–287 (2023).
60. A Cardellini, et al., Unsupervised data-driven reconstruction of molecular motifs in simple to complex dynamic micelles. *J. Phys. Chem. B* **127**, 2595–2608 (2023).
61. L Schaedel, et al., Lattice defects induce microtubule self-renewal. *Nat. Phys.* **15**, 830–838 (2019).
62. S Baoukina, D Rozmanov, DP Tieleman, Composition fluctuations in lipid bilayers. *Biophys. J.* **113**, 2750–2761 (2017).
63. SJ Marrink, HJ Risselada, S Yefimov, DP Tieleman, AH De Vries, The martini force field: coarse grained model for biomolecular simulations. *J. Phys. Chem. B* **111**, 7812–7824 (2007).
64. S Lloyd, Least squares quantization in pcm. *IEEE Trans. Inf. Theory* **28**, 129–137 (1982).
65. G Lukat, J Kruger, B Sommer, Apl@ voro: a voronoi-based membrane analysis tool for gromacs trajectories. *J. chemical information modeling* **53**, 2908–2925 (2013).
66. RL Biltonen, D Lichtenberg, The use of differential scanning calorimetry as a tool to characterize liposome preparations. *Chem. Phys. Lipids* **64**, 129–142 (1993).
67. S Baoukina, E Mendez-Villuendas, DP Tieleman, Molecular view of phase coexistence in lipid monolayers. *J. Am. Chem. Soc.* **134**, 17543–17553 (2012).
68. R García Fernández, JL Abascal, C Vega, The melting point of ice i h for common water models calculated from direct coexistence of the solid-liquid interface. *J. Chem. Phys.* **124**, 144506 (2006).
69. R Capelli, F Muniz-Miranda, GM Pavan, Ephemeral ice-like local environments in classical rigid models of liquid water. *J. Chem. Phys.* **156**, 214503 (2022).
70. A Offei-Danso, A Hassanali, A Rodriguez, High-Dimensional Fluctuations in Liquid Water: Combining Chemical Intuition with Unsupervised Learning. *J. Chem. Theory Comput.* **18**, 3136–3150 (2022).
71. B Monserrat, JG Brandenburg, EA Engel, B Cheng, Liquid water contains the building blocks of diverse ice phases. *Nat. Commun.* **11**, 5757 (2020).
72. M Fitzner, GC Sosso, SJ Cox, A Michaelides, Ice is born in low-mobility regions of supercooled liquid water. *Proc. Natl. Acad. Sci.* **116**, 2009–2014 (2019).
73. E Aprà, F Baletto, R Ferrando, A Fortunelli, Amorphization mechanism of icosahedral metal nanoclusters. *Phys. Rev. Lett.* **93**, 065502 (2004).
74. PJ Steinhardt, DR Nelson, M Ronchetti, Bond-orientational order in liquids and glasses. *Phys. Rev. B* **28**, 784 (1983).
75. M Garzoni, et al., Effect of H-Bonding on Order Amplification in the Growth of a Supramolecular Polymer in Water. *J. Am. Chem. Soc.* **138**, 13985–13995 (2016).
76. CMA Leenders, et al., Supramolecular polymerization in water harnessing both hydrophobic effects and hydrogen bond formation. *Chem. Commun.* **49**, 1963–1965 (2013).
77. TA Wassenaar, HI Ingólfsson, RA Bockmann, DP Tieleman, SJ Marrink, Computational lipidomics with insane: a versatile tool for generating custom membranes for molecular simulations. *J. Chem. Theory Comput.* **11**, 2144–2155 (2015).
78. JLF Abascal, E Sanz, R García Fernández, C Vega, A potential model for the study of ices and amorphous water: Tip4p/ice. *J. Chem. Phys.* **122**, 234511 (2005).
79. M Matsumoto, T Yagasaki, H Tanaka, GenIce: Hydrogen-Disordered Ice Generator. *J. Comput. Chem.* **39**, 61–64 (2018).
80. B Hess, C Kutzner, D van der Spoel, E Lindahl, GROMACS 4: Algorithms for Highly Efficient, Load-Balanced, and Scalable Molecular Simulation. *J. Chem. Theory Comput.* **4**, 435–447 (2008).
81. AP Thompson, et al., LAMMPS - a flexible simulation tool for particle-based materials modeling at the atomic, meso, and continuum scales. *Comput. Phys. Commun.* **271**, 108171 (2022).
82. H Wang, L Zhang, J Han, W E, DeePMD-kit: A deep learning package for many-body potential energy representation and molecular dynamics. *Comput. Phys. Commun.* **228**, 178–184 (2018).
83. RP Gupta, Lattice relaxation at a metal surface. *Phys. Rev. B* **23**, 6265–6270 (1981).
84. A Savitzky, MJE Golay, Smoothing and differentiation of data by simplified least squares procedures. *Anal. Chem.* **36**, 1627–1639 (1964).
85. P Virtanen, et al., SciPy 1.0: Fundamental Algorithms for Scientific Computing in Python. *Nat. Methods* **17**, 261–272 (2020).
86. JH Ward Jr, Hierarchical grouping to optimize an objective function. *J. Am. Stat. Assoc.* **58**, 236–244 (1963).

Supporting Information for

Detecting dynamic domains and local fluctuations in complex molecular systems *via* timelapse neighbors shuffling

Martina Crippa, Annalisa Cardellini, Cristina Caruso and Giovanni M. Pavan

Giovanni M. Pavan
E-mail: giovanni.pavan@polito.it

This PDF file includes:

Figs. S1 to S19
Table S1
Legends for Movies S1 to S3
SI References

Other supporting materials for this manuscript include the following:

Movies S1 to S3

SYSTEM	r_{cut} [Å]	# of g(r)$_m$ peaks	Length of MD[ns]	# of sampled frames	Sampling Δt [ns]	LENS center
DPPC/DIPC Lipids	16	3	10000	1001	10	PO4
F-NP/H Micelle	16	3	3000	3001	1	HEAD (CoM)
DPPC Lipids 293K	16	3	1000	1001	1	PO4
DPPC Lipids 273K	16	3	1000	1001	1	PO4
DPPC Lipids 323K	16	3	1000	1001	1	PO4
TIP4P/Ice Water	7.4	3	50	500	0.1	OW
Cu(210) 700K	4.9	3	150	502	0.3	Cu
Cu(211) 600K	4.9	3	150	502	0.3	Cu
Au-NP 200K	4.4	2	1000	1000	1	Au
BTA	15.8	3	20000	20001	1	BENZ (CoM)

Table S1. Setup details of all the LENS analyses conducted in this work.

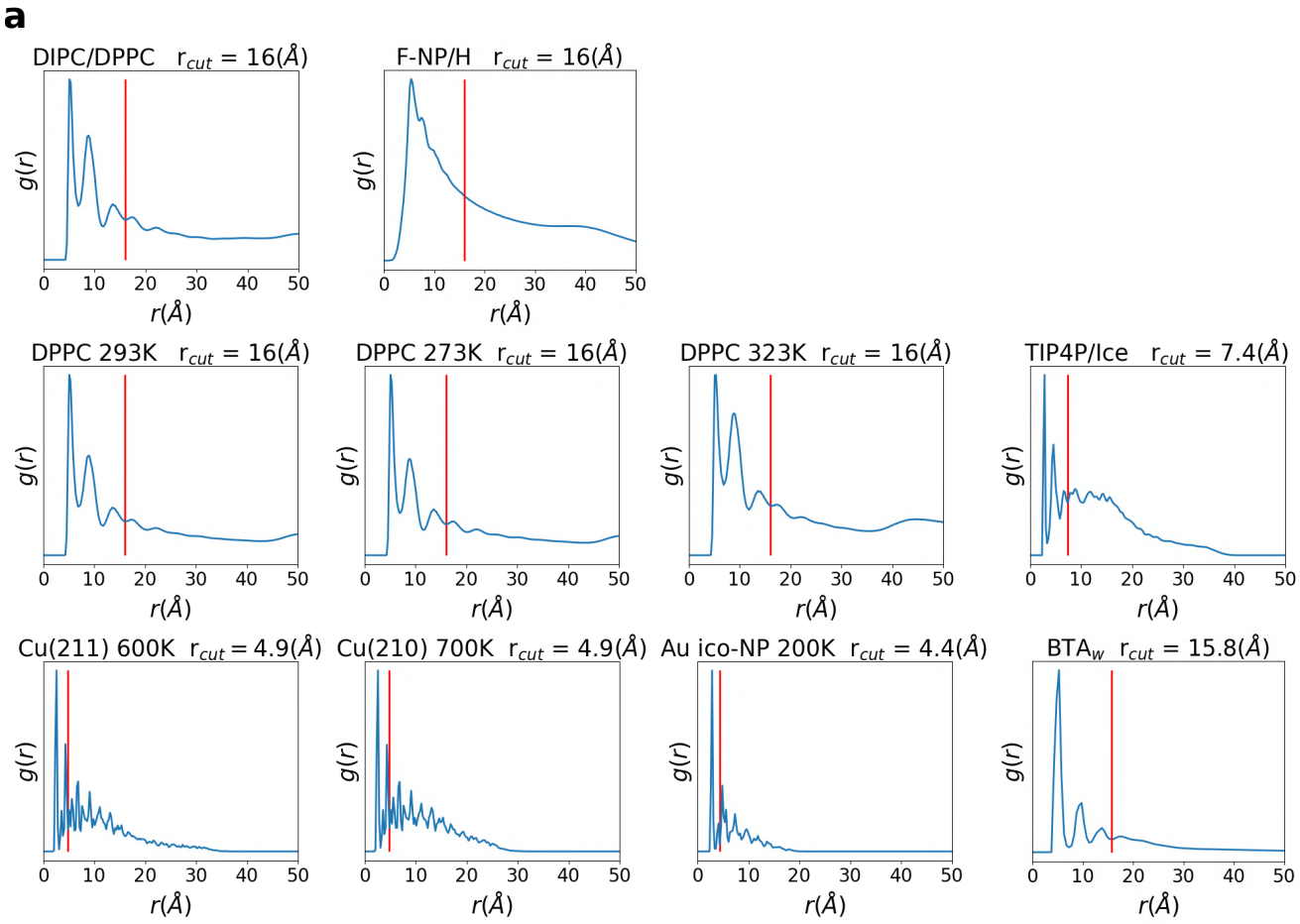

Fig. S1. (a) Radial distribution functions (g(r)) and cut-off radius r_{cut} for all systems.

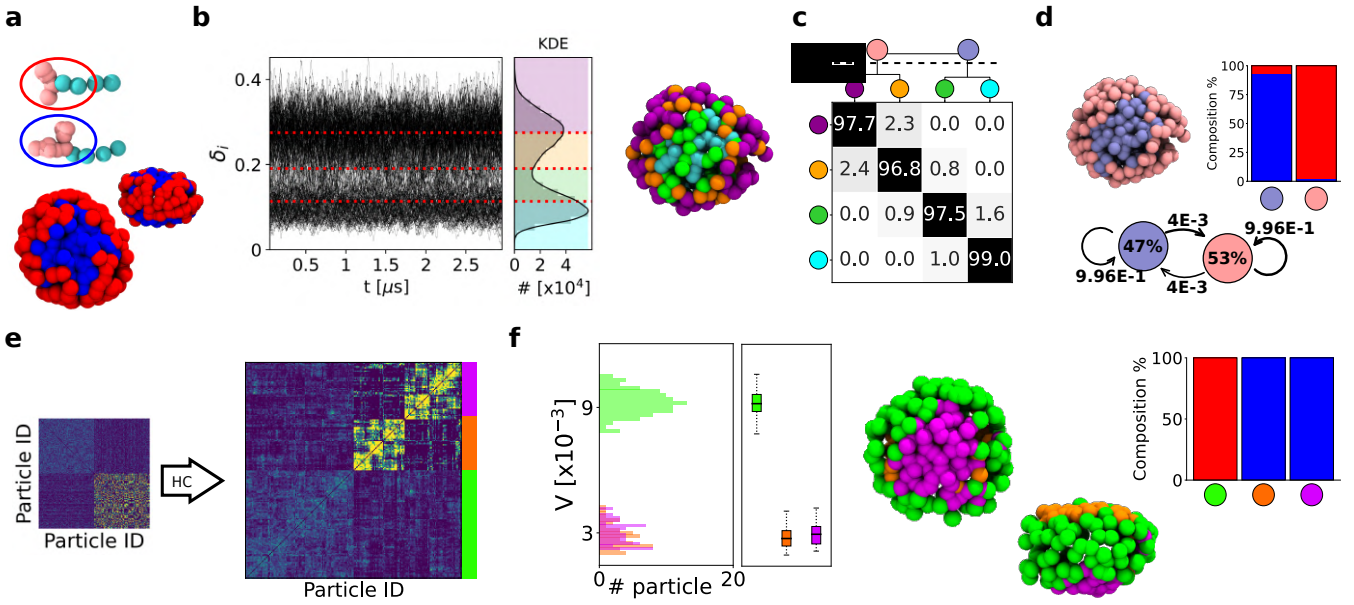

Fig. S2. LENS analysis of fluid-like systems. (a) Bicomponent amphiphile micelle composed of 100 **H** surfactants and 100 **F-NP** surfactants colored in red and blue, respectively. (b) Time-series of LENS signals, $\delta_i(t)$, with the Kernel Density Estimate (KDE) of LENS distribution classified into four clusters (left). MD snapshot of the micelle colored according to their clusters of belonging (right). (c) Inter-clusters normalized transition probability matrix. The p_{ii} and p_{ij} matrix entries indicate the $\%$ probability that molecules with LENS signal typical of a cluster i remain in that dynamical environment or move to another one j (with different dynamics) in Δt. Hierarchical grouping of the dynamically-closer clusters (dendrogram cutting) is reported on top of the matrix, and it provides two macroclusters, merging cyan and green on one hand, and orange and purple on the other hand. (d) MD snapshot of the micelle colored according to macroclusters in (c): light-blue identifying **F-NP** surfactants, pink identifying **H** surfactants (top-left). Cluster composition histogram (top-right) and interconversion diagram (bottom) with the transition exchange probabilities and the cluster population percentages (within colored circle). (e) HC analysis of the D^T matrix identifying three main clusters (green, purple, orange). (f) *Variability*, V, analysis of the clusters: distributions, median (first and third quartiles), maximum and minimum values (whiskers). The green have higher V than the orange and magenta clusters (left). MD snapshot front and lateral view of the micelle colored according the HC clustering of D^T matrix (middle). Cluster composition histogram (top-right): the green cluster is made of **H** surfactants (in red in (a)), while the orange and magenta ones correspond to the **F-NP** surfactants (in blue in (a)).

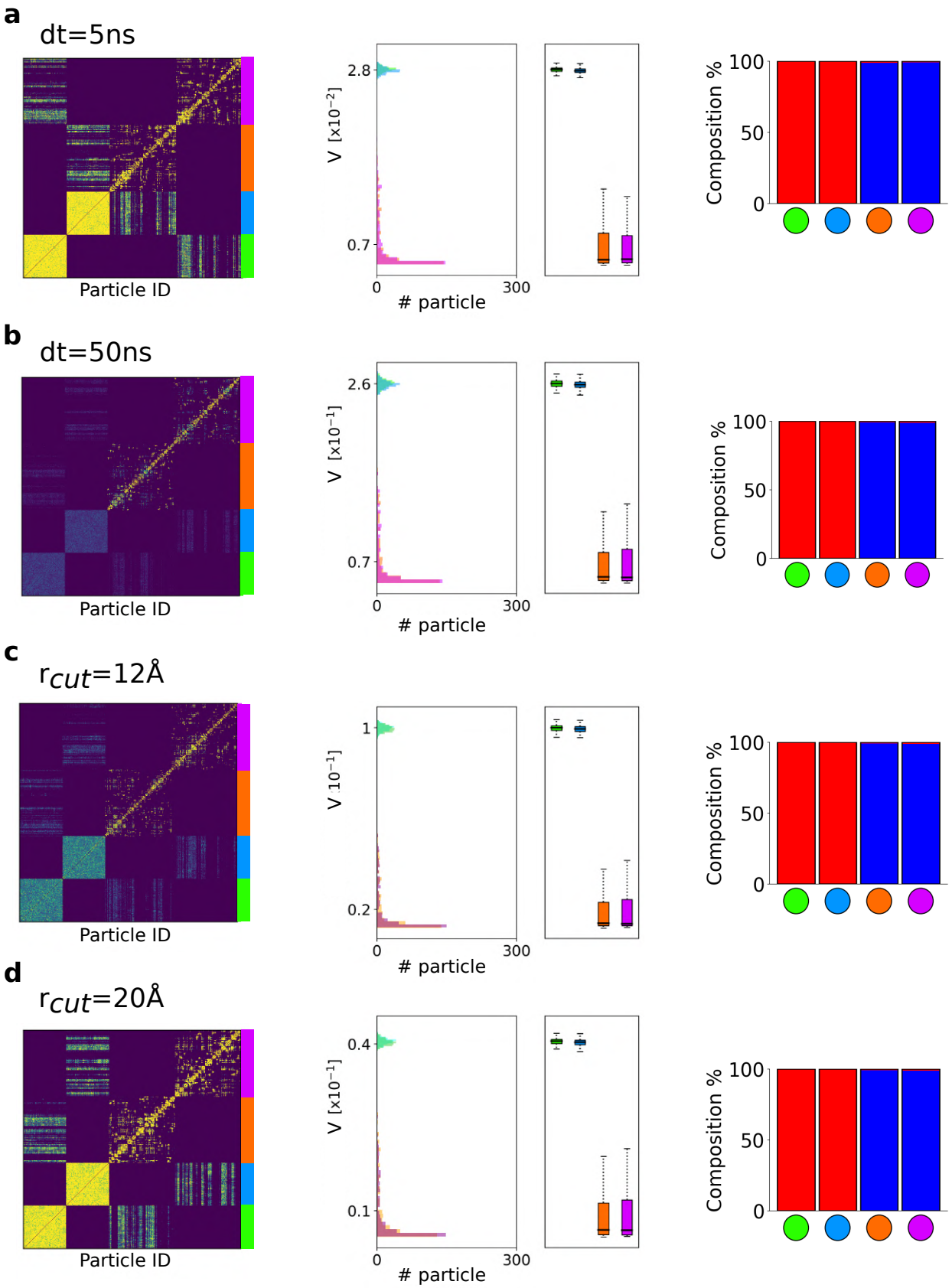

Fig. S3. Statistical analysis for **DIPC**/**DPPC** lipid bilayer, varying sampling step Δt or neighborhood cutoff radius r_{cut} while keeping all the other parameters as reported in Table S1. (a) $\Delta t = 5$ ns, (b) $\Delta t = 50$ ns, (c) $r_{cut} = 12$ Å and (d) $r_{cut} = 20$ Å.

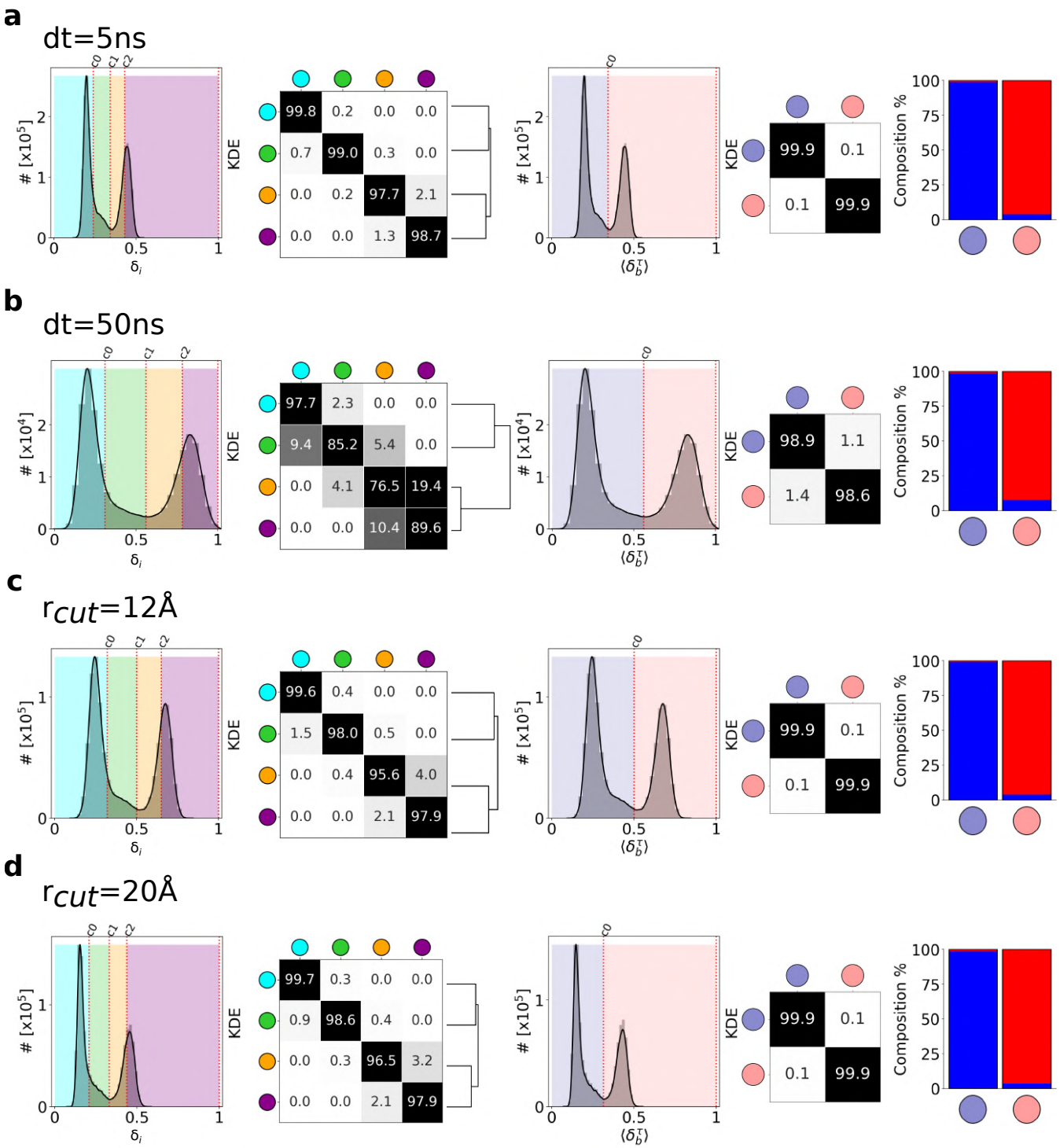

Fig. S4. LENS analysis for **DIPC**/**DPPC** lipid bilayer, varying sampling step Δt or neighborhood cutoff radius r_{cut} while keeping all the other parameters as reported in Table S1. (a) $\Delta t = 5$ ns, (b) $\Delta t = 50$ ns, (c) $r_{cut} = 12$ Å and (d) $r_{cut} = 20$ Å. Comparison of these results demonstrates the robustness of the LENS analysis: while the microscopic information captured by the analysis may change with the Δt or r_{cut}, a "zoom out" via grouping the adjacent microclusters based on the hierarchical dendrograms provide consistent results (right).

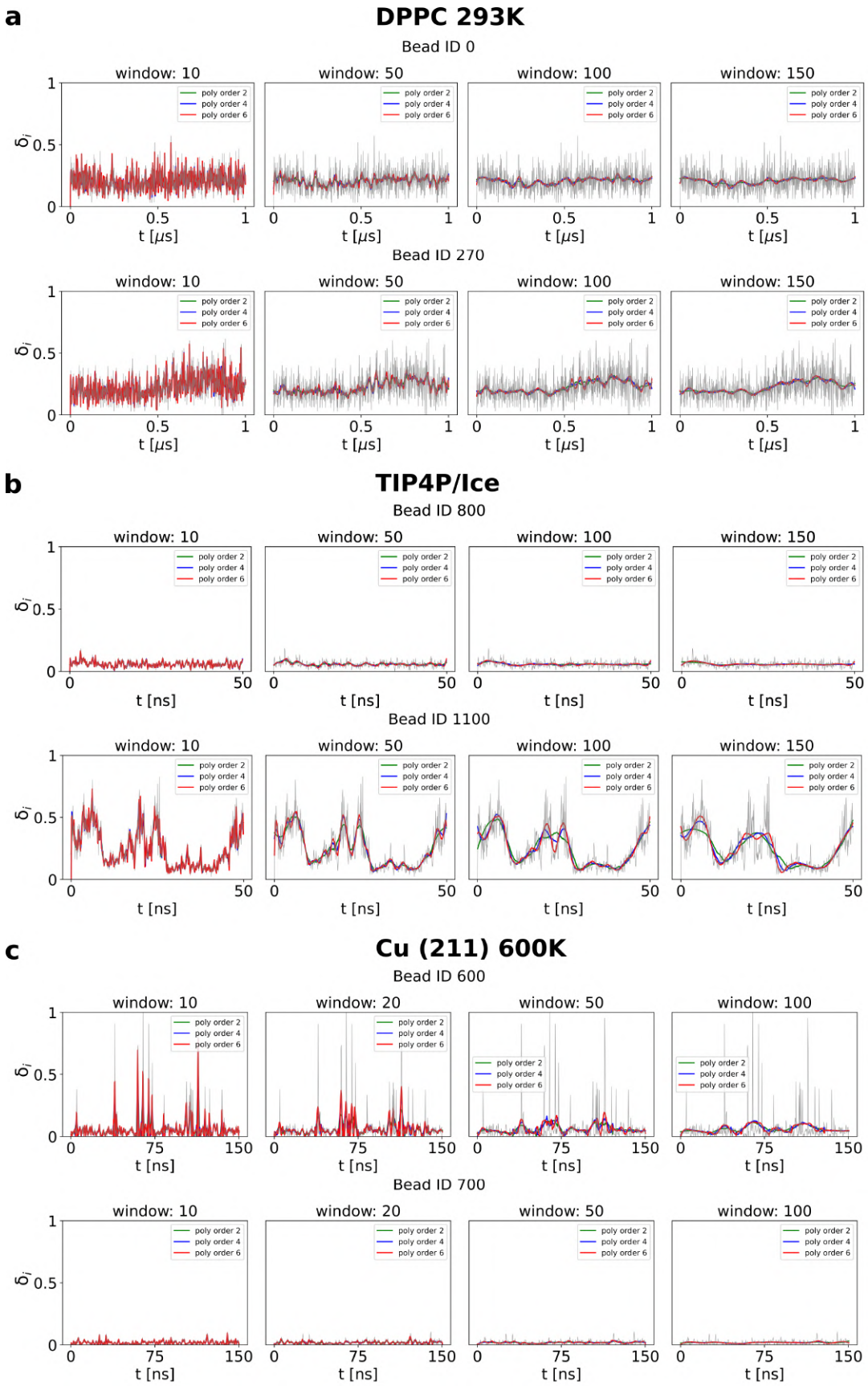

Fig. S5. Parameter study for applying the Savitzky–Golay filter varying both window interval and polynomial order for two bead examples each of (a) **DPPC** $293\ \mathrm{K}$, (b) **TIP4P/Ice** water and (c) **Cu (211)** copper slab.

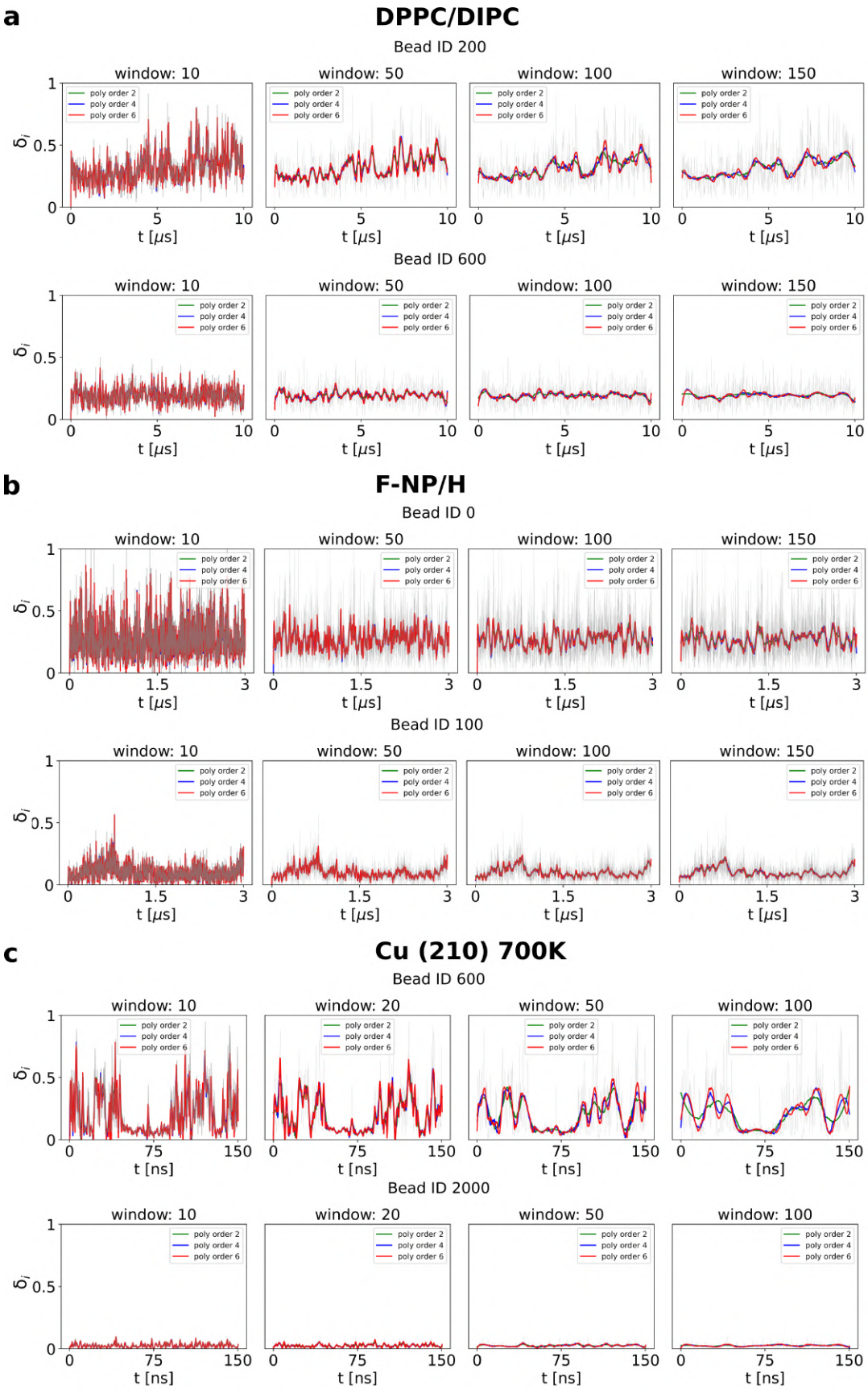

Fig. S6. Parameter study for applying the Savitzky–Golay filter varying both window interval and polynomial order for two bead examples each of (a)**DPPC**/**DIPC** lipid bilayer, (b) **F-NP**/**H** micelle and (c) **Cu (210)** copper slab.

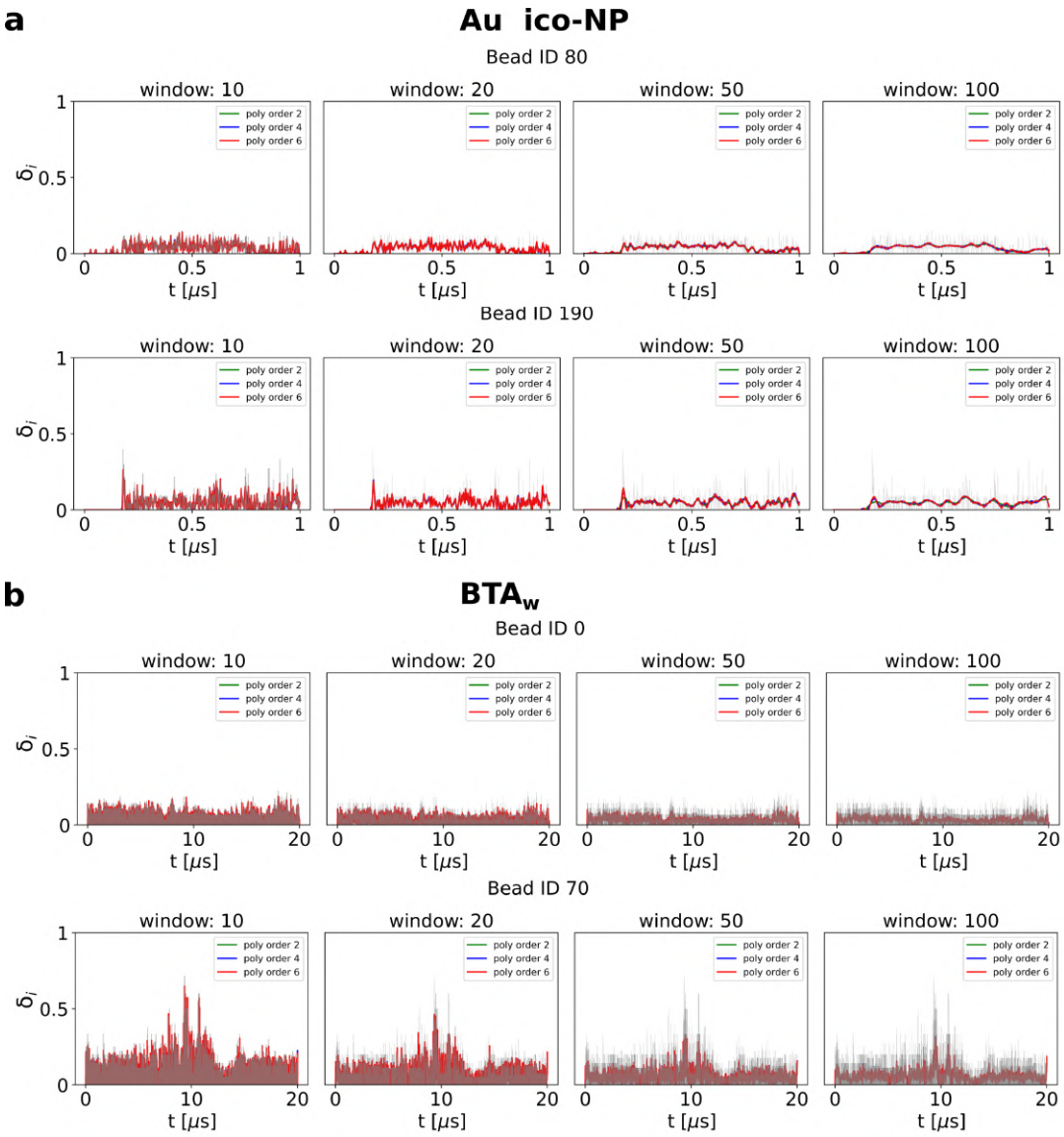

Fig. S7. Parameter study for applying the Savitzky–Golay filter varying both window interval and polynomial order for two bead examples each of (a) **Au-NP** and (b) **BTA**.

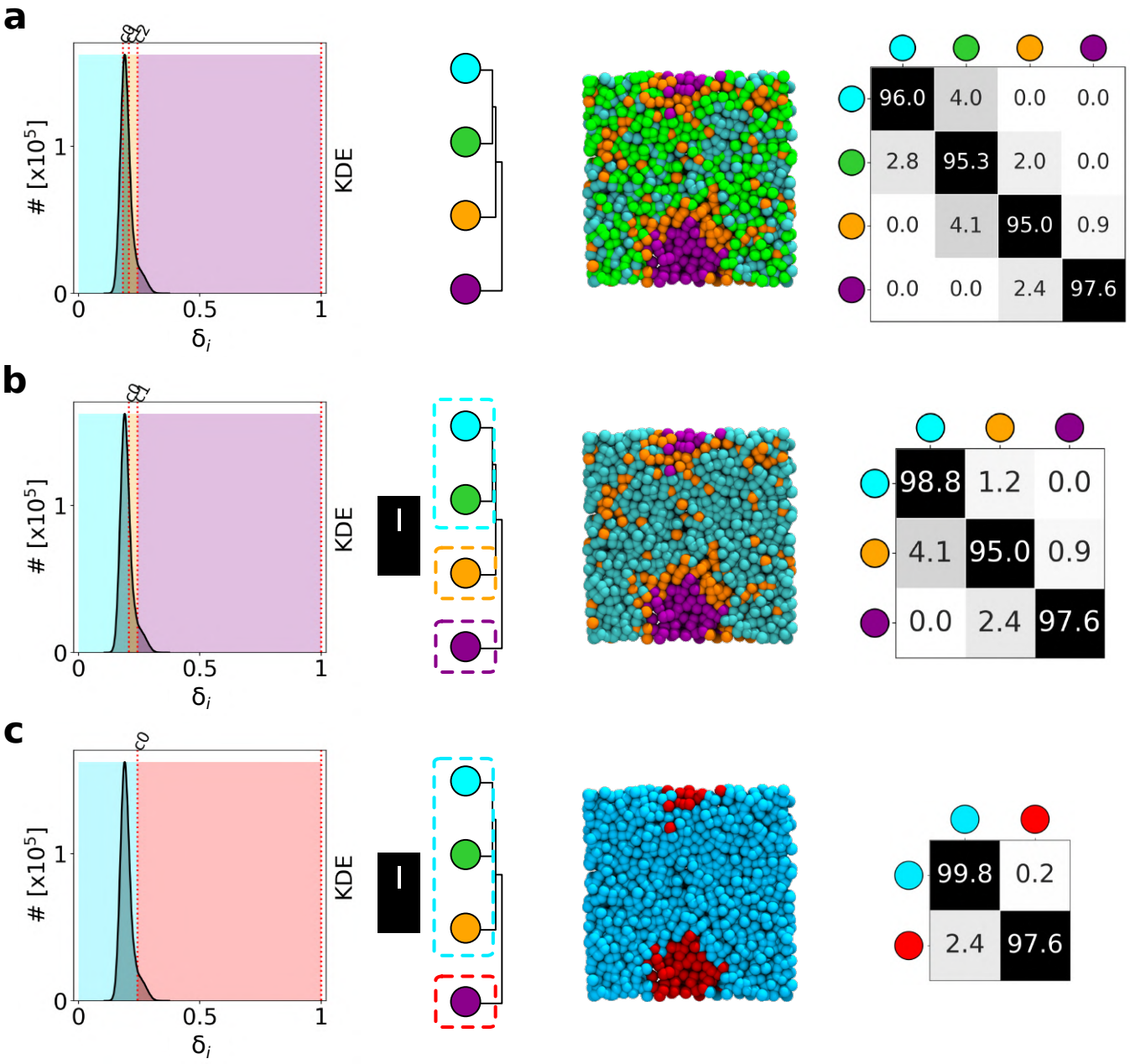

Fig. S8. DPPC Lipid bi-layer at $T = 293$ K: merging LENS clusters at different levels (no merging (a), two clusters merged into one (b) and three clusters merged into one (c)) following the hierarchy given by the dendrogram, example snapshot and transition probability matrix.

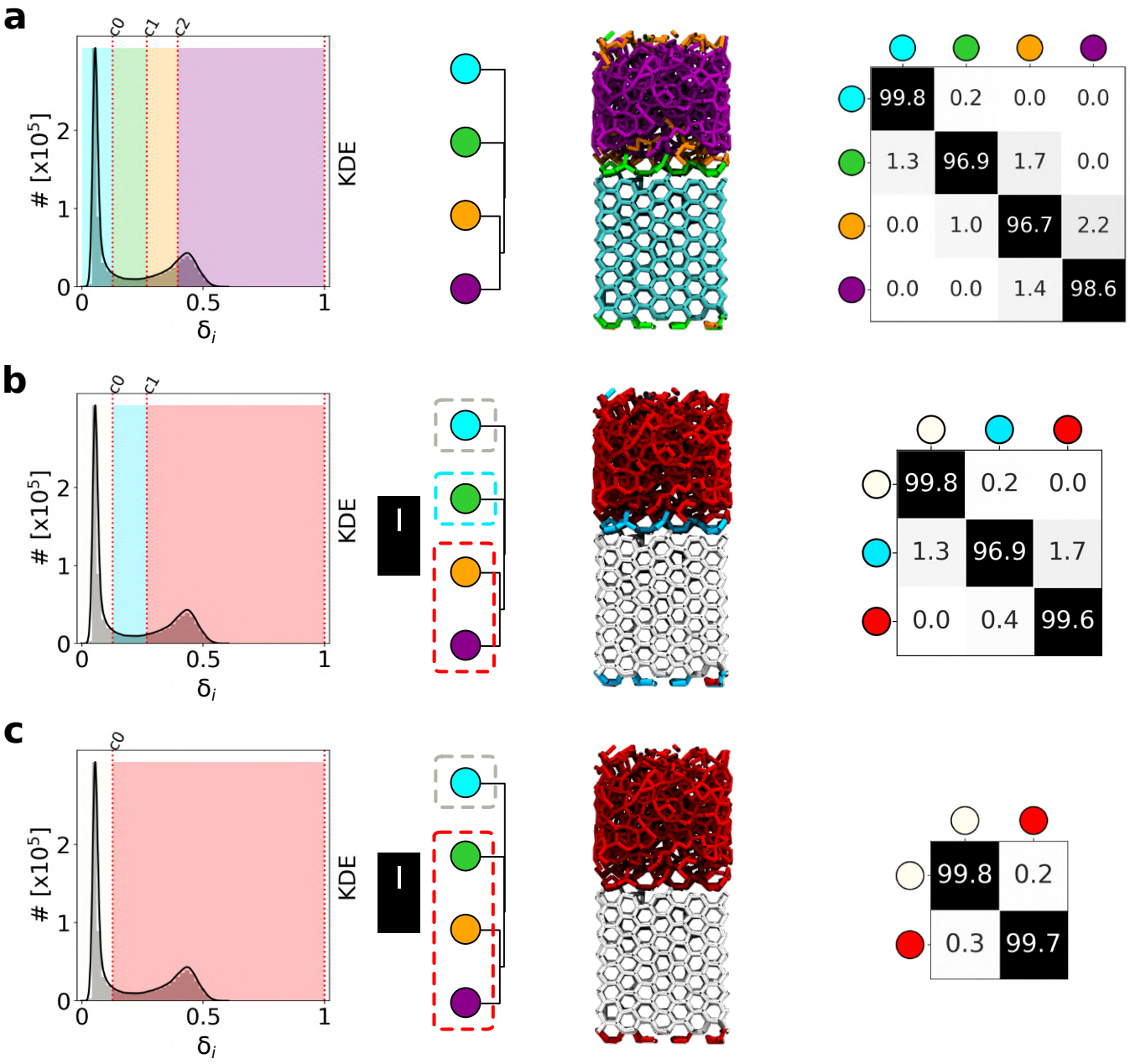

Fig. S9. TIP4P/Ice froze/melted water: merging LENS clusters at different levels (no merging (a), two clusters merged into one (b) and three clusters merged into one (c)) following the hierarchy given by the dendrogram, example snapshot and transition probability matrix.

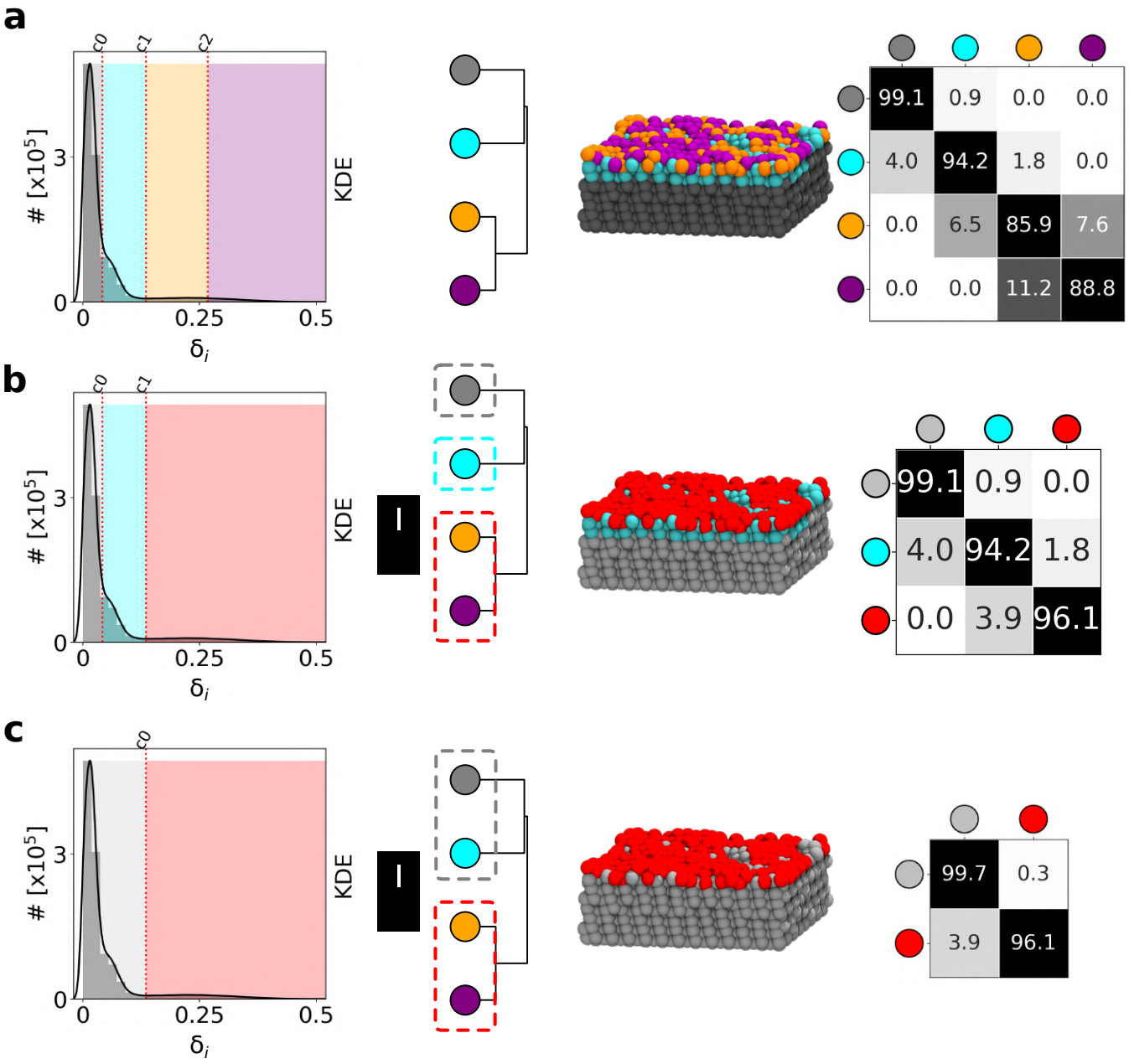

Fig. S10. Cu (210) copper slab at $T = 700$ K: merging LENS clusters at different levels (no merging (a), two clusters merged into one (b) and four clusters merged into two (c)) following the hierarchy given by the dendrogram, example snapshot and transition probability matrix.

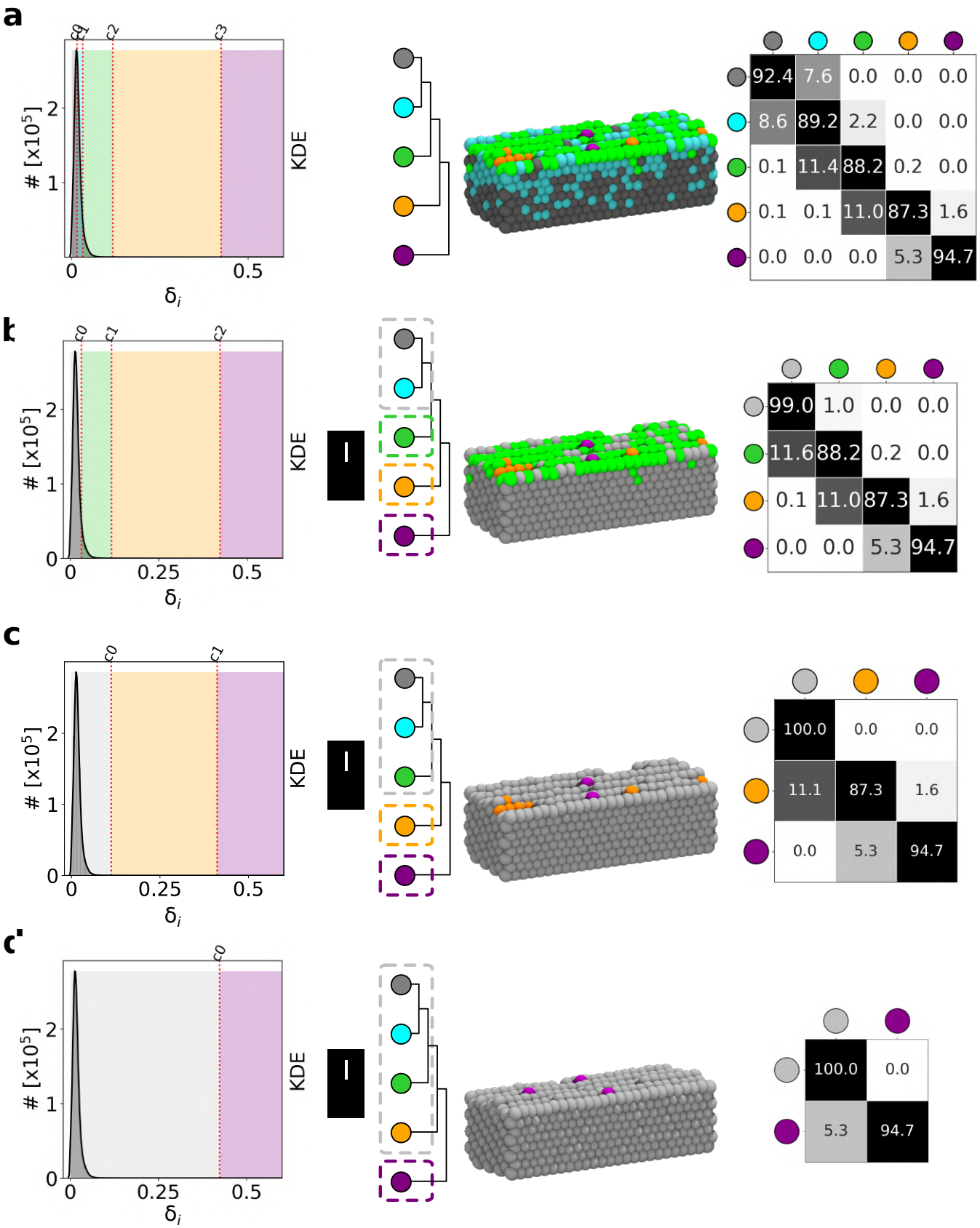

Fig. S11. Cu (211) copper slab at $T = 600$ K: merging LENS clusters at different levels (no merging (a), two clusters merged into one (b), three clusters merged into one (c) and four clusters merged into one (d)) following the hierarchy given by the dendrogram, example snapshot and transition probability matrix.

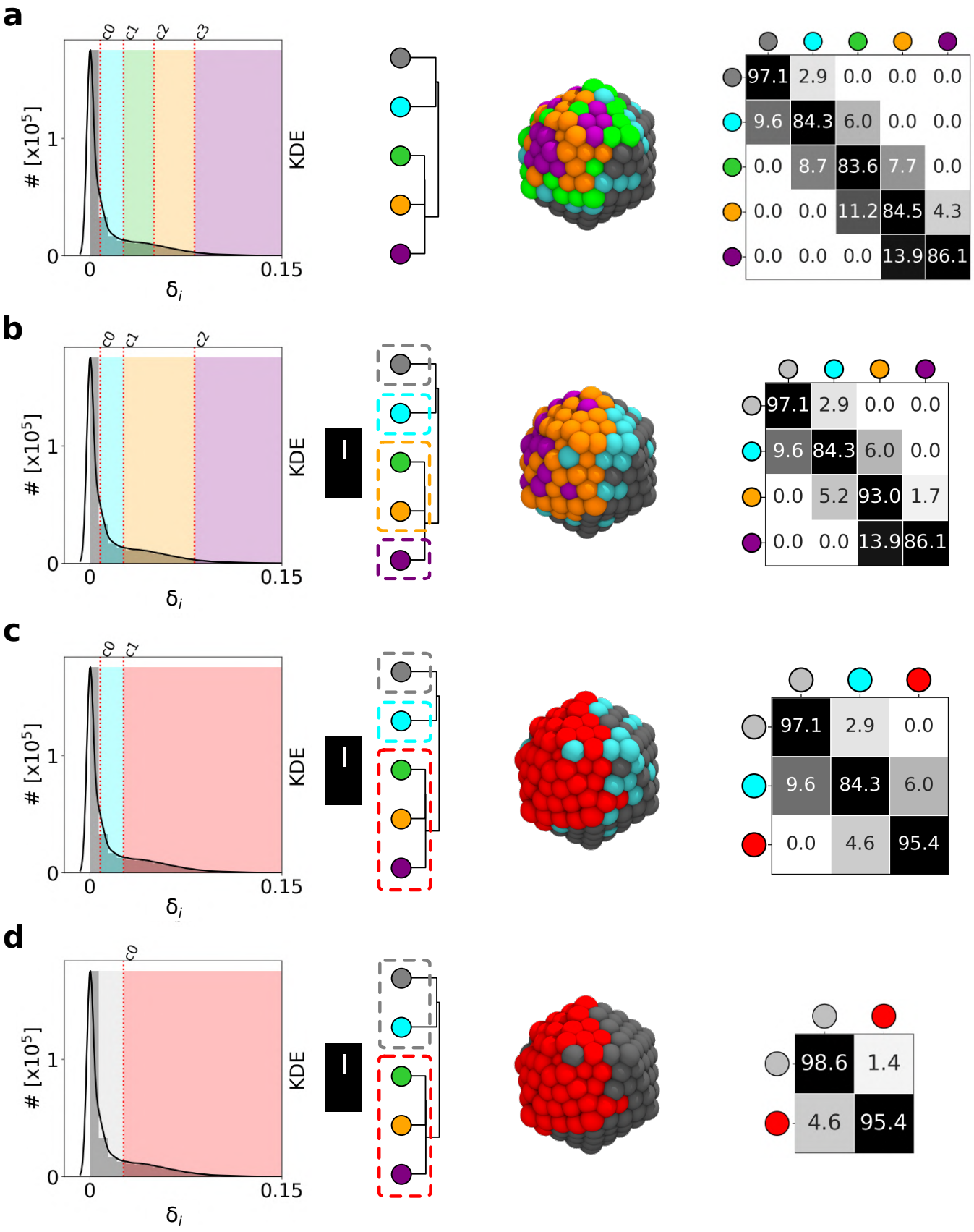

Fig. S12. Au-NP nanoparticle $T = 200$ K: merging LENS clusters at different levels (no merging (a), two clusters merged into one (b), three clusters merged into one (c) and three clusters and two clusters merged into two (d)) following the hierarchy given by the dendrogram, example snapshot and transition probability matrix.

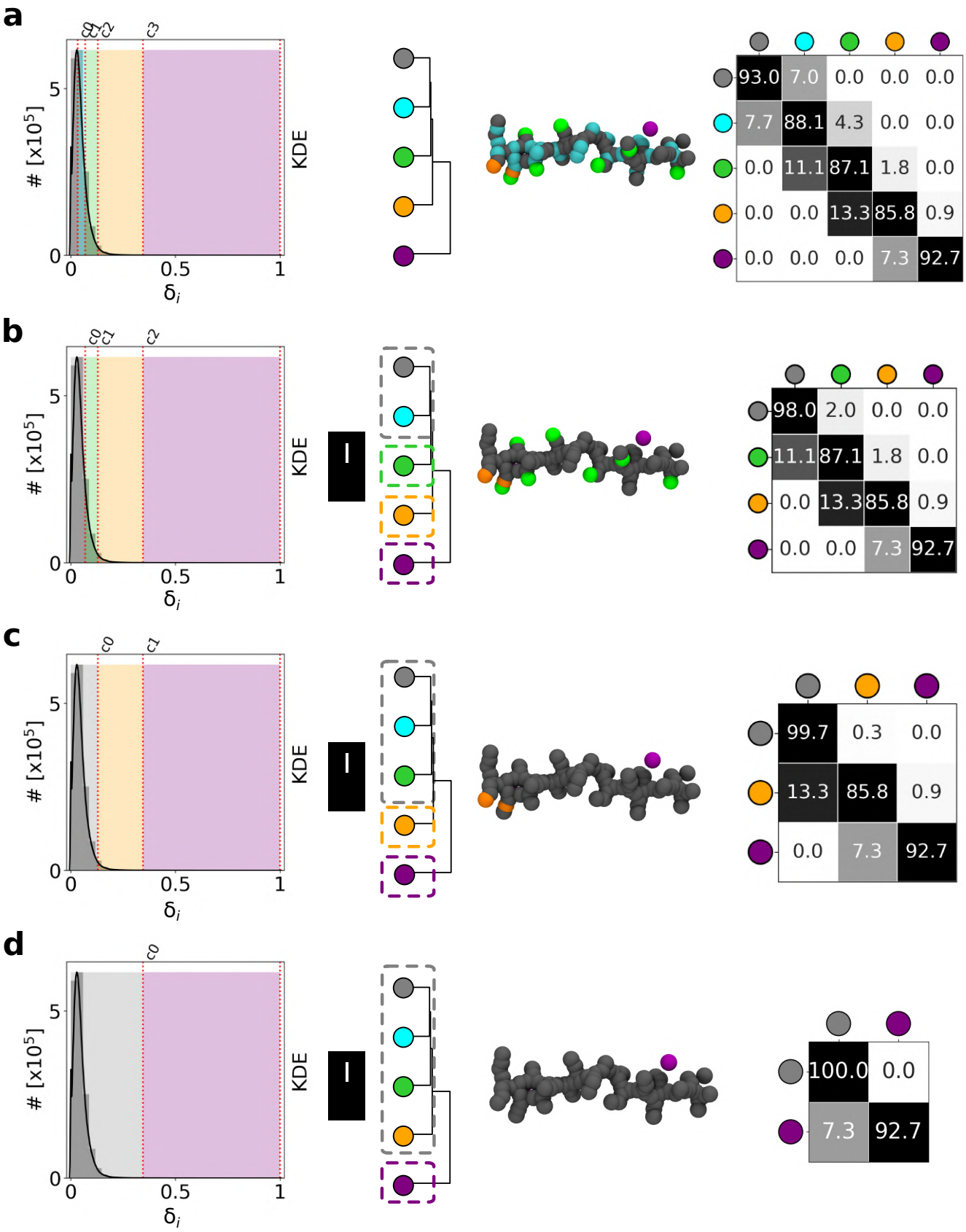

Fig. S13. BTA fiber: merging LENS clusters at different levels (no merging (a), two clusters merged into one (b), three clusters merged into one (c) and four clusters merged into one (d)) following the hierarchy given by the dendrogram, example snapshot and transition probability matrix.

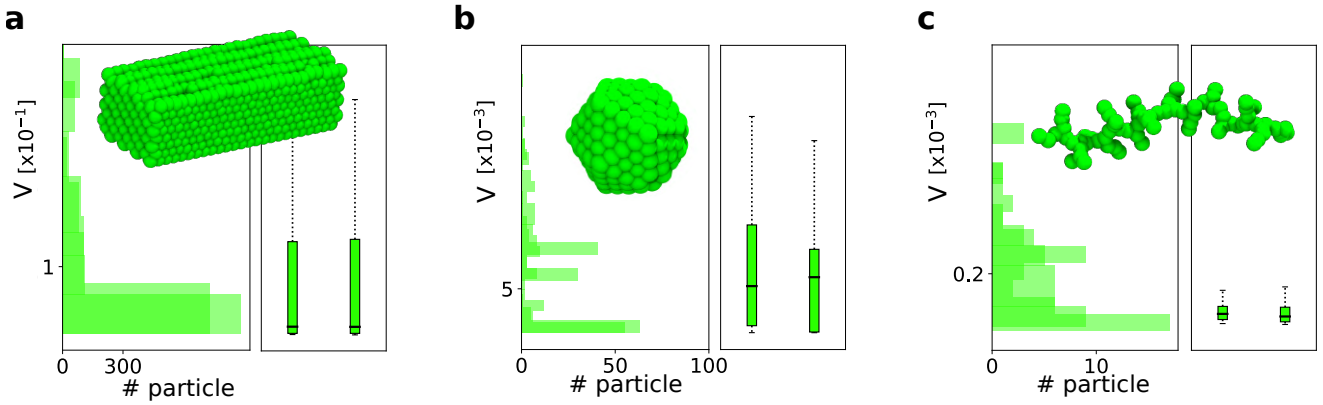

Fig. S14. Time-independent statistical analysis for **Cu (211)** copper slab at $T = 600$ K(a), **Au-NP** nanoparticle at $T = 200$ K(b) and **BTA** fiber (c): when the system is characterized by discrete and fluctuation-like dynamics, a time-indepentend averaged analysis fails to recognize patterns which are not statistically relevant. For example, in the systems reported above, the two clusters identified by HC have identical variability V and they can be classified as the same cluster.

1. Voronoi analysis

The data reported in Figure S15 show a comparison between LENS- vs. Voronoi-based clustering in case of the lipid-species compartmentalization seen in a DIPC-DPPC lipid bilayer at 280K (which is expected experimentally (1)). Figure S15a (left) shows a top view of the lipid bilayer where it is clear how the DIPC (red lipids) and DPPC (blue lipids) are self-segregated in this system (see Figure 2). The LENS-based clustering identifies two main dynamic domains: a light violet cluster (smallest LENS values), fitting almost exactly with the blue DPPC lipids, and a pink cluster (largest LENS values), fitting essentially with the red DIPC lipids (see the composition bar plot in Figure S15a). Figure S15a shows the Voronoi analysis estimated with APL@Voro v3.0 (2) where each Voronoi area/tassel (i.e. A_v), is colored on the basis of its size. Visually, such a comparison shows how the Voronoi analysis of the lipid qualitatively correlates with the LENS results. Small values of A_v - and hence, a more compact aggregation of the lipids – qualitatively correspond to the less dynamic light-violet LENS cluster (with the blue DPPC lipids, in gel-phase in such conditions). On the other hand, large Voronoi areas roughly corresponds to the more dynamic pink LENS cluster (red DIPC lipids, in liquid phase in these conditions). A systematic study of the effect of setting the lipid threshold areas (A_t) for the Voronoi classification of lipids in liquid vs. in gel phase has revealed how the detection of different dynamical domains based on structural factors (Voronoi) is less robust than the one that can be obtained by directly monitoring the microscopic dynamics in the neighborhood of each lipid in these systems (via LENS). Figure S15b reports four reference-choices of the A_t and the consequently obtained results: Top-left: $A_t = 0.561\text{nm}^2$ is the average Area Per Lipid (APL) computed on the entire lipid bilayer under study. The representation of clusters in violet and yellow and their composition (Figure S15b top left) demonstrates a reliable classification in terms of cluster size (lipids population in %) and an overall good qualitative matching with the lipid species reported above in blue and red. The violet cluster mostly matches with the light violet LENS-cluster (blue lipids), while the yellow domain mainly corresponds to the pink LENS-domain (red lipids). Obviously, the same happens to the correlation between the yellow (liquid) and violet (gel) Voronoi clusters, which correlate in good approximation with the red DIPC and blue DPPC lipids, but less precisely than what obtained with LENS (panel a). As additional cases, we also report the results obtained with an $A_t = 0.574\text{nm}^2$. This is threshold area value providing the best agreement with the LENS analysis. As it is clear, the results are very similar to those obtained with $A_t = 0.561\text{nm}^2$: between the two analysis there is correlation, but not perfect agreement. As the last two demonstrative cases, we show what results are obtained by decreasing or increasing over the A_t threshold value (bottom-left and -right respectively). The results of these analyses demonstrate how in such cases the Voronoi analysis becomes less accurate in capturing the two liquid and gel phases present in this system (the bilayer appearing more and more liquid/gel while using lower-and-lower/larger-and-larger A_t threshold values).

Figure S16 shows the same comparison between LENS- and Voronoi-based clustering in the case of the liquid phase nucleation and liquid-gel phase coexistence in the DPPC lipid bilayer at 293K. Figure S16a left shows the LENS-based clustering of DPPC lipids at 293K. As described in the main text of our paper, the red and cyan LENS clusters identify well the liquid and gel phases (large and small LENS signals/variability respectively). This is further validated in the table of Figure S16c, reporting the Mean Square Displacement (MSD) of the DPPC lipids in the cyan (gel) and red (liquid) LENS clusters at 293K (2nd row). By comparing the first two rows of the table it is clear the MSD of the lipids in the cyan and red LENS domains are found in the same order of magnitude of the MSD expected for lipids in the gel phase (cyan LENS lipids' MSD similar to the MSD of DPPC lipids at 273K, where they are fully in gel phase) and in the liquid phase (red LENS lipids' MSD in the same order of the MSD of DPPC lipids at 323K, where they are fully in the liquid phase). On the other hand, a 2D Voronoi analysis is found less efficient in discriminating the two phases, and the microscopic nucleation and coexistence of one phase into the other. Figure S16a (right) shows the Voronoi tessellation estimated with APL@Voro v3.0 (2). As in new Figure S15, in order to quantitatively distinguish the two phases, and thus to classify each Voronoi polyhedron area as liquid or gel, in Figure S16 we compare the results obtained using four different threshold Voronoi area values, namely $A_t = 0.478\text{nm}^2$, $A_t = 0.510\text{nm}^2$, $A_t = 0.400\text{nm}^2$, $A_t = 0.600\text{nm}^2$, and the relative classification of DPPC lipids into liquid ($A_v > A_t$) or gel ($A_v < A_t$) phases, colored in yellow and violet respectively. $A_t = 0.478\text{nm}^2$ corresponds to the average Area Per Lipid (APL) computed for this DPPC bilayer at 293K (very close to the experimental one of $APL = 0.473\text{nm}^2$ for DPPC at 293K, see Figure S16b, top left). In this case, as demonstrated by the composition bar plot, the yellow and violet Voronoi clusters are equally populated, and both mostly composed of cyan LENS lipids (in the gel phase). This is also demonstrated by the MSD values obtained for the two yellow and violet clusters (3rd row in the table of Figure S16c), showing how the two detected Voronoi clusters do not fit with a liquid vs. gel environments (MSD close in both cases to that of a gel system). As done for the previous case, we also optimized the choice of the threshold Voronoi area to maximize the correspondence between the LENS and Voronoi clusters – case with $A_t = 0.510\text{nm}^2$ in Figure S16b (top right). Despite slightly improved results, also in this case we clearly observe how a structural-based, Voronoi analysis is less efficient and accurate than our LENS analysis in detecting the two distinct phases. The last results of Figure S16 demonstrate also how increasing/decreasing further the At generates worse results, tending to detect one single phase. These outcomes demonstrate how, in such a case – where, in particular, the reduced statistical presence of the nucleating phase (compared to the statistical weight of the dominant phase) makes it even more difficult to detect it – LENS demonstrates a remarkable efficiency in achieving this goal, while a structural-based analysis (such as e.g. the 2D Voronoi tessellation used herein) is in comparison less efficient.

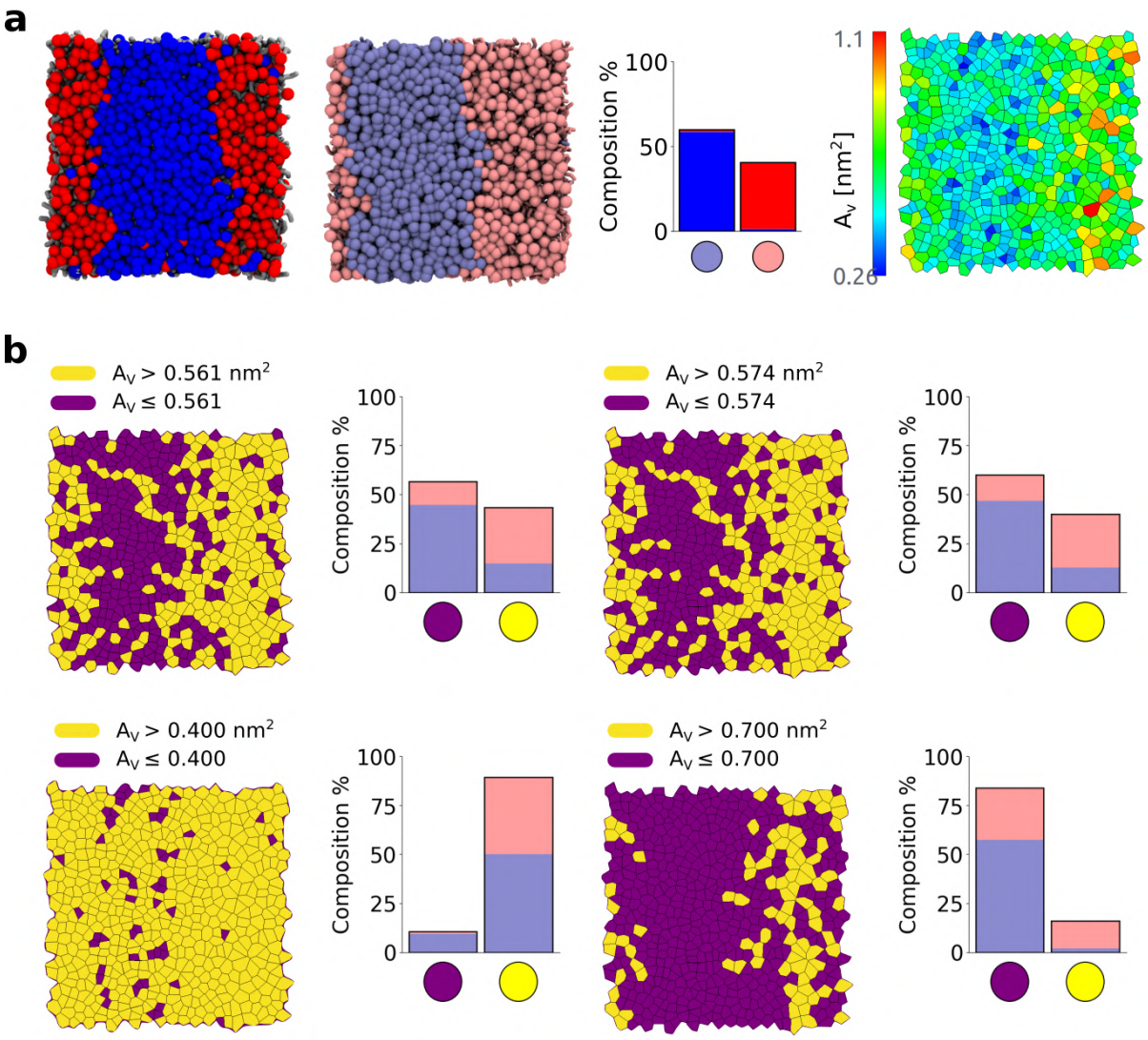

Fig. S15. Voronoi analysis for **DIPC-DPPC** lipid bilayer at $T = 280\mathrm{K}$. (a) Left: Top view of the bicomponent lipid bilayer colored by component (DIPC in red, DPPC in blue) and by LENS cluster assignment (light violet and pink clusters identify small and high LENS values: respectively, gel and liquid phases). The overlap of DIPC-DPPC components with LENS clusters and their composition percentages are shown in the histogram. Right: example of the Voronoi tessellation where each Voronoi area A_v, is colored based on its size. (b) Voronoi clustering based on a selected threshold area At equal to: the average Area Per Lipid in the system (top left: $A_t = 0.561\mathrm{nm}^2$), the value of A_t maximizing the match between Voronoi and LENS analyses (top right), and results obtained with smaller and higher At values (bottom left and right respectively). Cluster color code: yellow for Voronoi area $A_v > A_t$ (liquid) and violet for $A_v \leq A_t$ (gel). The histograms show the LENS/Voronoi clusters matching for all cases. While the results show that an optimized Voronoi analysis matches qualitatively well with the LENS one, the results show how LENS detects in more accurate and robust way the fact that the two gel and liquid domains correspond to segregated DPPC and DIPC domains, consistently with the experimental evidence.(1)

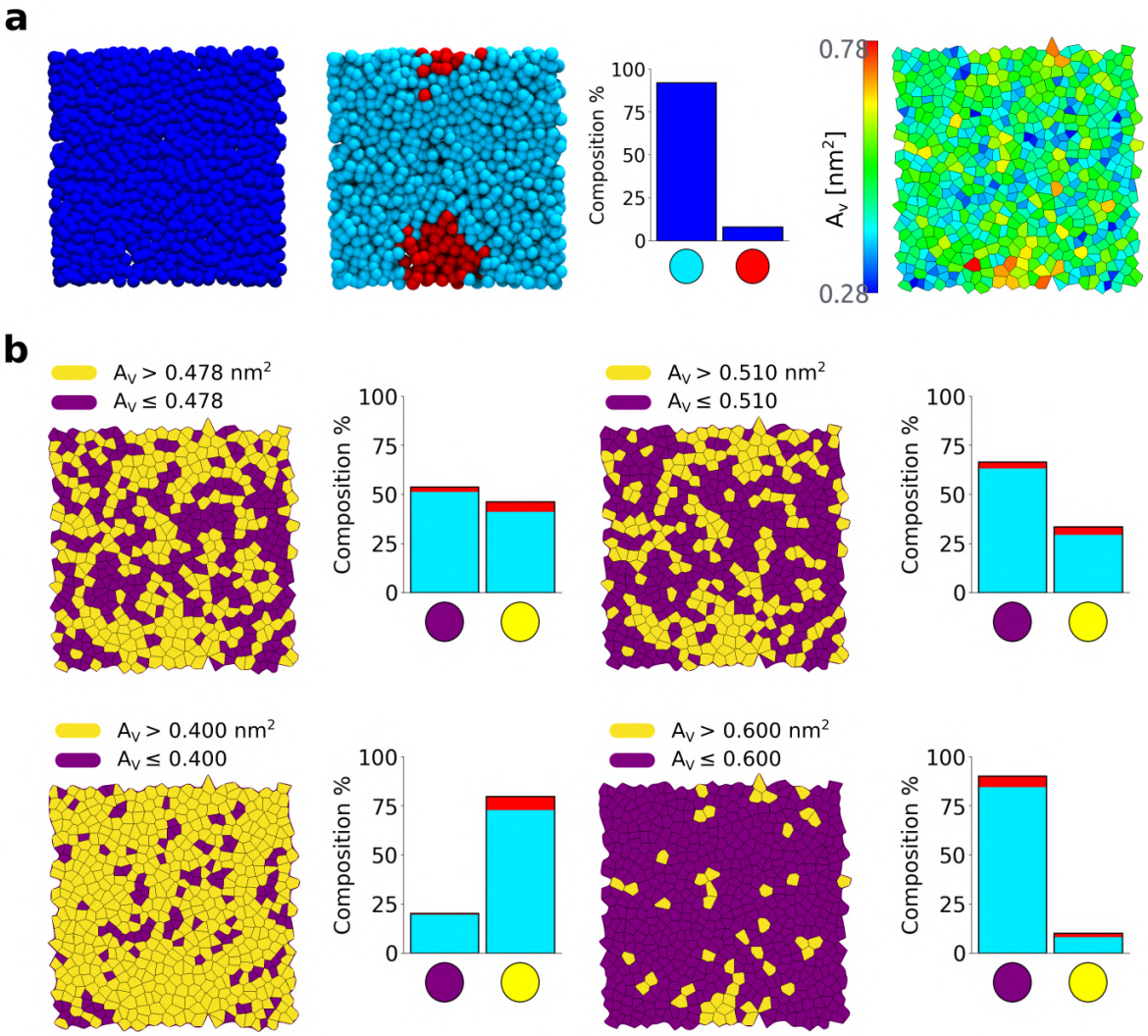

c

	DPPC 273K (gel)	DPPC 323K (liquid)	DPPC 293K
MSD [Å^2]	25.96	391.66	40.88
	DPPC 293K LENS cyan cluster	**DPPC 293K LENS red cluster**	
MSD [Å^2]	35.93	100.00	
	DPPC 293K $A_v \leq 0.478$Å^2	**DPPC 293K** $A_v > 0.478$Å^2	
MSD [Å^2]	38.26	43.93	

Fig. S16. Voronoi analysis for liquid phase nucleation in the gel phase and liquid/gel phases coexistence in a **DPPC** lipid bilayer at $T = 293\mathrm{K}$. (a) Left: Top views of the lipid bilayer colored according to the DPPC species (blue lipids) and by LENS cluster assignment (cyan and red clusters identify small and high LENS values, respectively). Right: example of the Voronoi tessellation where each Voronoi area A_v, is colored based on its size. (b) Voronoi clustering based on a selected threshold area A_t equal to: the Area Per Lipid of the system (top left), optimized area to obtain the best match between Voronoi and LENS clusters (top right), and too small and too high A_t values (bottom). Cluster color code: yellow for Voronoi area $A_v > A_t$ and violet for $A_v \leq A_t$. The histogram shows LENS/Voronoi clusters overlapping and their composition percentages for each At threshold. (c) Table reporting the Mean Squared Displacement (MSD) analysis of DPPC lipids in a bilayer configuration at $273\mathrm{K}$ (gel), $323\mathrm{K}$ (liquid) and $293\mathrm{K}$ (phases coexistence) – computed with a stride $10\mathrm{ns}$ – comparing the MSD of the lipids in the LENS or Voronoi clusters with, e.g., the MSD expected for lipids in full gel and liquid phase. The obtained results demonstrate how LENS capture well the presence of liquid and gel environments in the lipid bilayer (e.g., MSD values of cyan and red LENS clusters in the same order of magnitude of those expected for gel or liquid DPPC lipid bilayers) and how, on the contrary, a standard Voronoi analysis is inefficient in this sense (similar MSD for violet and yellow clusters, close to that of gel bilayers).

2. Steinhardt and SOAP analysis

In Figure S17a, we have plotted the Steinhardt (3) parameters *q4* and *q6* related to each atom of **Cu(211)** slab at $T = 600$K (see the MD snapshot reported on the right). HDBSCAN clustering (4) has been carried out on the cloud of order parameter data and two main domains are detected. As it is clear in Figure S17, a blue cluster corresponds to the atoms belonging to the topmost edges of the ideal (0K) Cu(211) surface, while all other atoms (bulk plus the other surface atoms) correspond to an orange cluster. Upon thermalization at 600K, a larger part of the surface atoms turns blue, meaning that they become less coordinated and ordered, and more dynamic (surface atoms that were orange in the ideal surface become more similar to the edge ones in terms of structure of their local neighborhood). This is sensible and not surprising, and it is in a sense a lower-resolution version of what it has been seen recently using a SOAP-based analysis.(5)

As an additional comparison, we also performed additional data-driven analyses on the same Cu surface based on SOAP (6) that allow in principle for a richer structural analysis of the atomic motifs that populate the surface (see Figure S17b). Such SOAP analysis has been conducted following to the same procedure recently used for the study of similar systems.(5) In this case, clustering of the SOAP data extracted from the MD trajectory of the **Cu(211)** surface at 600K shows many more colors, and a richer distinction of the different atomic environments that constitute the surface. As also seen in the Steinhardt analysis, it is clear that upon thermalization the surface becomes more "disordered/dynamic" than at 0K (the number of colors – i.e., number of different SOAP environments – increases).

A very similar result is obtained for the **Au-NP** at $T = 200$K. We have also computed the Steinhardt bond order parameters for the **Au-NP** at 200K, as shown in Figure S18a, left. The cluster representation based on *q4* and *q6* parameters demonstrates that the analysis is extremely accurate to reconstruct the geometrical environments in the Au NP, detecting e.g. edges, faces, vertexes of the icosahedral NP, and showing how upon heating to 200K the surface environments intermix while the surface becomes dynamic (see Figure S18). Also in this case, this result is very similar to that obtained recently with a SOAP classification.(7)

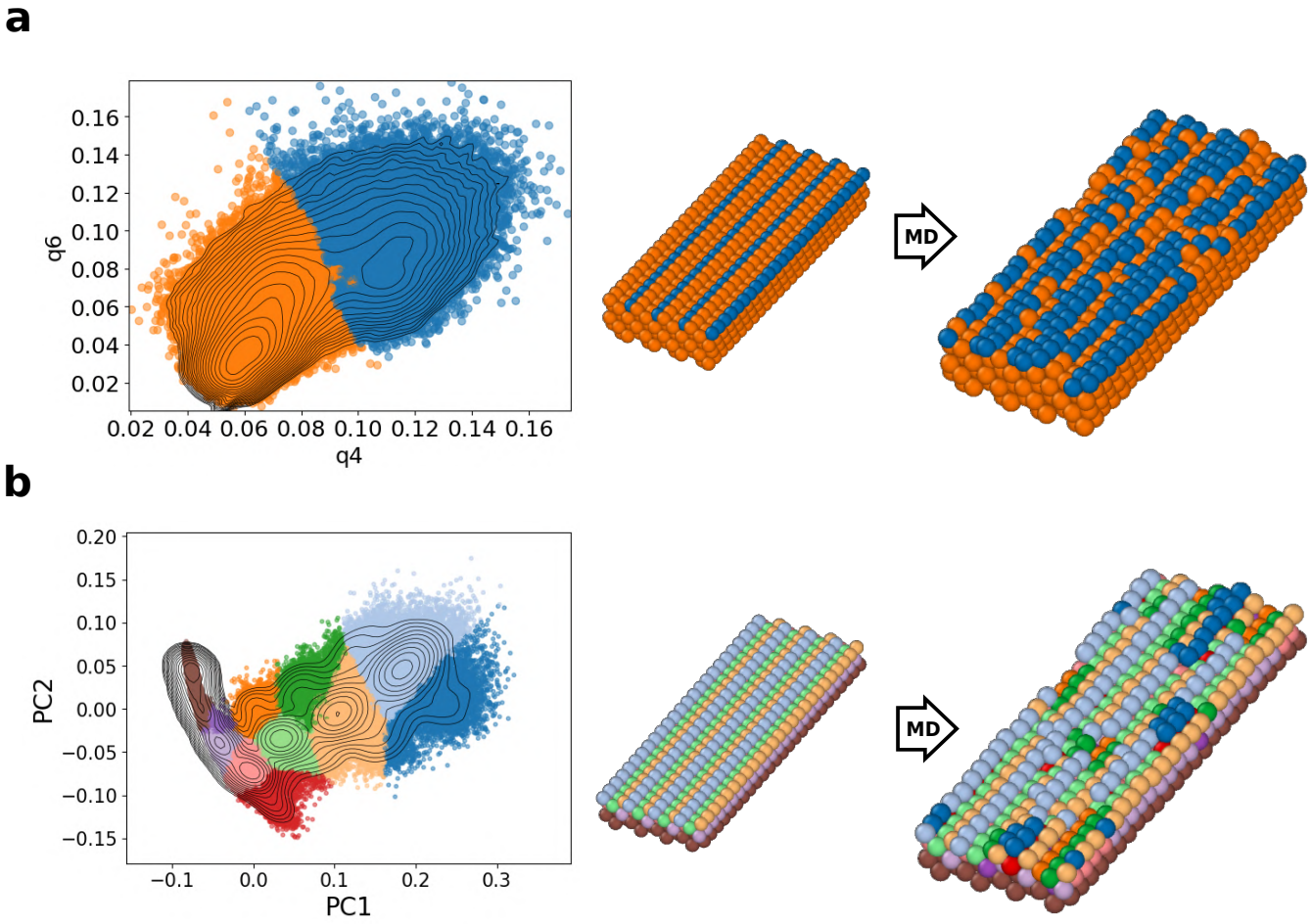

Fig. S17. (a) Steinhardt analysis for **Cu(211)** copper surface slab at $T = 600\mathrm{K}$: *q4* and *q6* order parameters are computed for each atom considering the environment within r_{cut} reported in Table S1; then HDBSCAN clustering (`min_cluster_size`=700,`min_samples`=20 with noise assignment (7)) is applied identifying two main structural environments: bulk and sub-surface (orange), surface (blue). (b) SOAP and clustering analysis for **Cu(211)** copper slab at $T = 600\mathrm{K}$. The high dimensional SOAP spectrum is computed for each atom considering the environment within r_{cut} reported in Table S1 and a Principal Component Analysis (PCA) is applied to reduce the high dimensional spectrum to four dimensions (cumulatively 99.7 % of the information is kept in the four PC, in Figure b left are reported the first two PC). Then HDBSCAN clustering (`min_cluster_size`=250, `min_samples`=2 with noise assignment (7)) is applied identifying eleven structural environments characterizing surface, sub-surface, bulk and structural deviation on the surface. While such analyses can capture a high-level of structural details, the dynamics information – obtained via, e.g., averaging the transitions between the detected atomic environments populating the surface (5) – makes it very difficult to detect sparse rare fluctuations that are important to understand the dynamical properties of such systems (see also LENS Movie S2).

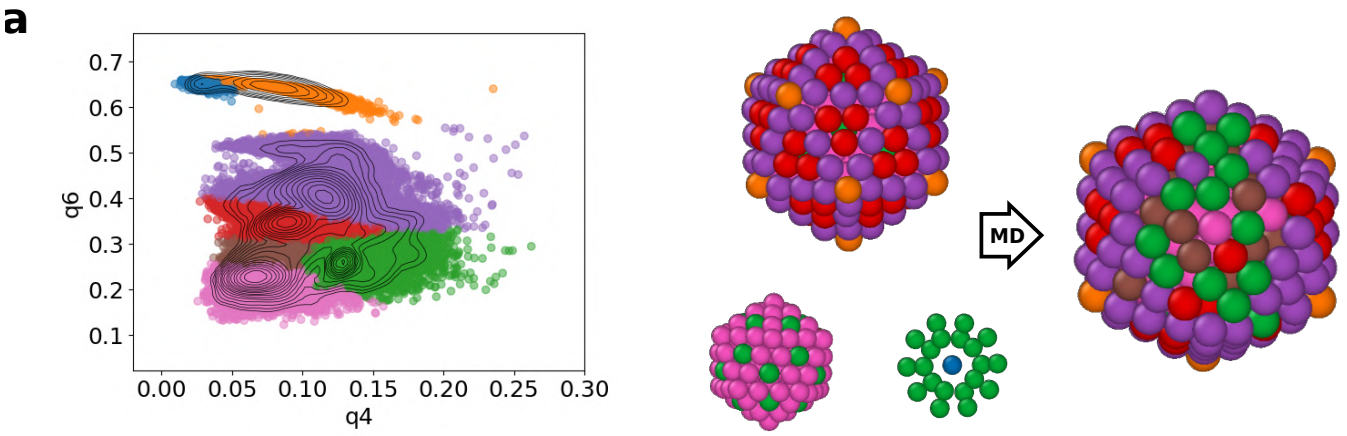

Fig. S18. (a) Steinhardt analysis for **Au-NP** nanoparticle at $T = 200\mathrm{K}$: *q4* and *q6* order parameters are computed for each atom considering the environment within r_{cut} reported in Table S1; then HDBSCAN clustering (`min_cluster_size`=700, `min_samples`=1 with noise assignment (7)) is applied identifying seven structural environments characterizing the surface (vertices, edges and faces) and bulk of the particle. While such structural analyses (e.g. Steinhardt or SOAP (6) can capture a high-level of structural details, the dynamics information reconstructed from them – obtained via, e.g., averaging the transitions between the detected atomic environments populating the surface (5)– makes it very difficult to detect local fluctuations and the effect that these have on the whole system dynamics. On the other hand, LENS shows that half of the Au NP surface becomes dynamic following to the transformation of one vertex into a rosette, while the other half preserves its reduced, crystalline-like vibrational behavior (see also LENS Movie S3).

3. Dynamical Propensity analysis

We have carried out a systematic comparison between LENS and the dynamical propensity (DP) descriptor developed in the group of Michaelides. (8) In order to apply the dynamical propensity to our ice-liquid water system, we computed for each water molecule the parameter DP:

$$DP_i = \left\langle \frac{\|r_i(t+\Delta t) - r_i)t)\|^2}{MSD} \right\rangle_{MDtraj} \quad [1]$$

where $r_i(t)$ is the position vector of molecule i at time t, Δt is the sampling time in our MD trajectory, and the MSD is the mean-square displacement of all oxygen atoms. It is worth noticing that in our case the ensemble average is estimated over the instantaneous displacements collected along the MD trajectory. After computing the DP values for all water molecules, we have estimated the probability density distribution P(DP) (see Figure S19), where two distinct peaks are clearly notable: $DP = 0.5$ and $DP = 2$, highlighting a low and high dynamical propensity of water molecules, respectively. Such result is evidently close to the LENS distribution in Figure 3, indicating a sort of correlation between the DP and LENS, and consequentially validating our descriptor. The resulting DP values are then classified selecting the thresholds both on the minimum of the P(DP) (a) and -+30% from the minimum of the P(DP)(b), obtaining two and three clusters respectively, as reported in Figure S19a and S19b, respectively. As evident from the MD snapshots, the DP-based clustering enables an explicit identification of ice (gray cluster), liquid (blue cluster) phases, and eventually the ice-liquid water interface (red clusters).

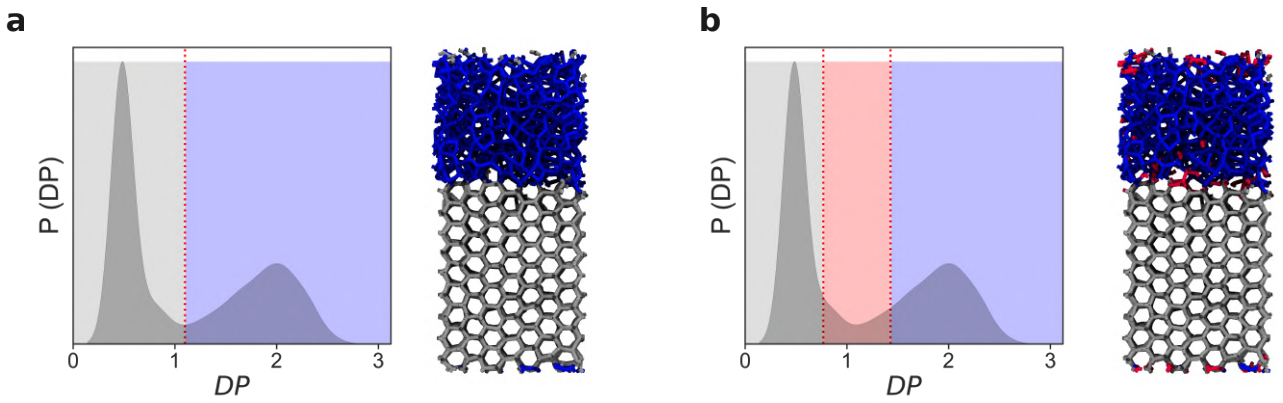

Fig. S19. Comparison with other state-of-the-art benchmark analyses: Probability density distribution of the Dynamical Property (DP)(8) computed for each water molecules included in the ice-liquid phase transition system. The resulting DP values are then classified selecting the thresholds both on the minimum of the P(DP) (a) and -+30% from the minimum of the P(DP)(b), obtaining two and three clusters respectively. The MD snapshots of water report the gray (ice phase), blue (liquid phase), and red (ice-liquid interface) clusters. These DP distributions are consistent with the averaged KDE distributions obtained from the LENS signals in Figure 3e in the main paper.

Movie S1. LENS analysis of gel-liquid phase coexistence in a DPPC lipid bilayer at 293 K of temperature. Atoms are colored based on their main LENS environment of belonging: liquid-phase lipids in red, gel-phase lipids in cyan.

Movie S2. LENS analysis of local dynamic transitions in a Cu(211) surface at 600 K of temperature. Atoms are colored based on their main LENS environment of belonging: static solid-phase atoms in gray, more dynamic surface edge atoms in orange, and fast-diffusing atoms in violet.

Movie S3. LENS analysis of a local sharp transition in a icosahedral Au-NP at 200 K of temperature. Atoms are colored based on their main LENS environment of belonging: crystalline/ordered domains in gray, solid but more dynamic atomic environments in cyan, increasingly dynamic local environments in orange and violet respectively. The movie shows how the LENS analysis detects the local transformation event of one icosahedron vertex (having 5-neighbor atoms) into a concave "rosette" (with 6-neighbor atoms).

References

1. S Baoukina, D Rozmanov, DP Tieleman, Composition fluctuations in lipid bilayers. *Biophys. J.* **113**, 2750–2761 (2017).
2. G Lukat, J Krüger, B Sommer, Apl@voro: A voronoi-based membrane analysis tool for gromacs trajectories. *J. Chem. Inf. Model.* **53**, 2908–2925 (2013).
3. PJ Steinhardt, DR Nelson, M Ronchetti, Bond-orientational order in liquids and glasses. *Phys. Rev. B* **28**, 784 (1983).
4. L McInnes, J Healy, S Astels, hdbscan: Hierarchical density based clustering. *J. Open Source Softw.* **2**, 205 (2017).
5. M Cioni, et al., Innate dynamics and identity crisis of a metal surface unveiled by machine learning of atomic environments. *J. Chem. Phys* **158**, 124701 (2023).
6. AP Bartók, R Kondor, G Csányi, On representing chemical environments. *Phys. Rev. B* **87**, 184115 (2013).
7. D Rapetti, et al., Machine learning of atomic dynamics and statistical surface identities in gold nanoparticles. ChemRxiv [Preprint] (2022) https://chemrxiv.org/engage/chemrxiv/article-details/63642e6aac45c7a2a9a45332.
8. M Fitzner, GC Sosso, SJ Cox, A Michaelides, Ice is born in low-mobility regions of supercooled liquid water. *Proc. Natl. Acad. Sci.* **116**, 2009–2014 (2019).